

This document is the Accepted Manuscript version of a Published Work that appeared in final form in Applied Catalysis A, General 591 (2020) 117381, after peer review and technical editing by the publisher. To access the final edited and published work see <https://doi.org/10.1016/j.apcata.2019.117381>

OXIDATION OF LEAN METHANE OVER COBALT CATALYSTS SUPPORTED ON  
CERIA/ALUMINA

A. Choya, B. de Rivas, J.R. González-Velasco, J.I. Gutiérrez-Ortiz, R. López-Fonseca

Applied Catalysis A, General 521 (2020) 117381

DOI: 10.1016/j.apcata.2019.117381

©2019. This manuscript version is made available under the CC-BY-NC-ND 4.0 license  
<https://creativecommons.org/licenses/by-nc-nd/4.0/>

1     **OXIDATION OF LEAN METHANE OVER COBALT CATALYSTS**  
2                     **SUPPORTED ON CERIA/ALUMINA**

3

4                     Andoni Choya, Beatriz de Rivas, Juan Ramón González-Velasco,  
5                     Jose Ignacio Gutiérrez-Ortiz, Rubén López-Fonseca\*

6

7

8                     Chemical Technologies for Environmental Sustainability Group,  
9                     Department of Chemical Engineering, Faculty of Science and Technology,  
10                    University of The Basque Country UPV/EHU, PO Box 644, E-48080 Bilbao, Spain

11

12

13                    \*Corresponding author:

14                    Phone: +34-94-6015985

15                    Fax: +34-94-6015963

16                    E-mail address: [ruben.lopez@ehu.eus](mailto:ruben.lopez@ehu.eus)

17

18 **ABSTRACT**

19 Cobalt (30%wt.) oxide catalysts supported over ceria-modified (3-18%wt.) alumina  
20 supports were examined for the combustion of lean methane. The prepared samples  
21 were characterised by wavelength dispersive X-ray fluorescence, N<sub>2</sub> physisorption, X-  
22 ray diffraction, Raman spectroscopy, X-ray photoelectron spectroscopy, transmission  
23 electron microscopy, temperature-programmed reduction with hydrogen and  
24 temperature-programmed reaction with methane. A significant enhancement of the  
25 activity was evidenced with respect to the catalyst supported over bare alumina, with an  
26 optimal cerium loading of 12%wt. and a resultant T<sub>50</sub> value of 480 °C. The ceria  
27 modification was found to induce a dual positive effect on the performance of the cobalt  
28 catalysts. On one hand, it acted as a physical barrier between deposited cobalt and  
29 alumina, thus inhibiting the cobalt-alumina interaction and the subsequent cobalt  
30 aluminate formation. On the other hand, the insertion of cerium ions in the spinel lattice  
31 led to a distortion of the structure that in turn resulted in an enhanced mobility of the  
32 oxygen species. The optimised catalyst exhibited a relatively good thermal stability for  
33 prolonged reaction time intervals (150 h) under dry conditions. The presence of water  
34 vapour markedly affected the catalytic performance although this negative effect was  
35 partially reversible.

36

37 *Keywords: methane oxidation, cobalt oxide, modified alumina, ceria, lattice distortion*

38

## 39 **1. Introduction**

40 Cobalt-based catalysts have been largely used as oxidation catalysts in numerous  
41 environmental applications including VOC abatement and combustion of soot [1,2]. In  
42 this context, the control of emissions from natural gas vehicles (unburned methane) over  
43 this class of metal oxides has been also explored [3-5]. The use of cobalt catalysts with  
44  $\text{Co}_3\text{O}_4$  as the main active phase is frequently considered as a cheaper viable alternative  
45 to expensive noble-metal based catalysts with a proven higher specific activity [6]. The  
46 notable activity of this metal oxide is related to its good redox properties, and in  
47 particular, the easiness that the cobalt ions possess to switch between its two oxidation  
48 states (+3 and +2), which provides oxygen species in the lattice with a high mobility [7].  
49 Since the oxidation of methane by these type of catalysts is deemed to occur via a Mars-  
50 van Krevelen mechanism, where the oxygen species from the spinel lattice are  
51 responsible for the oxidation reaction [8,9], these redox properties are crucial for the  
52 activity of  $\text{Co}_3\text{O}_4$ -based catalysts, to the point that even catalysts with poor textural and  
53 structural properties can exhibit a relatively good performance [10,11]. Consequently,  
54 when proposing an efficient strategy for designing highly active  $\text{Co}_3\text{O}_4$  catalysts it is  
55 extremely important to maintain the structure and redox properties of the spinel as intact  
56 as possible.

57 The most commonly applied enhancing strategy is to support the cobalt oxide over the  
58 surface of a porous media, in order to disperse it and increase the amount of the  
59 available active surface area. Generally, this option produces catalysts with high  
60 specific surface areas and a small crystallite size of  $\text{Co}_3\text{O}_4$ , but it presents a major  
61 drawback in the form of a strong cobalt-support interaction that often negatively affects  
62 the redox properties of the cobalt oxide [12,13]. More specifically, when the support is  
63 alumina, this cobalt-support interaction usually provokes a partial reduction of  $\text{Co}^{3+}$  ions

64 to  $\text{Co}^{2+}$  and their subsequent fixation in the alumina lattice, which leads to the formation  
65 of cobalt aluminate ( $\text{CoAl}_2\text{O}_4$ ) [14]. The cobalt ions fixed in this phase lose almost all  
66 their mobility and cannot revert to the +3 oxidation state at moderate temperatures  
67 ( $< 600\text{ }^\circ\text{C}$ ), and therefore are rendered inactive for the oxidation reaction [15].

68 A possible solution to this problem is to modify the alumina support with a metallic  
69 promoter, prior to the deposition of cobalt species, in order to increase its stability and  
70 reduce its propensity to interact with the cobalt oxide deposited over it. This promoter  
71 can be added during the synthesis of the alumina support itself. Thus, Liotta et al. [16]  
72 found that adding Ba during the synthesis of  $\text{Al}_2\text{O}_3$  by a sol-gel method inhibited solid  
73 state diffusion of the  $\text{Co}^{2+}$  ions into the alumina after Co deposition. On the other hand,  
74 Cheng et al. [17] reported that the incorporation of a fourth element during the synthesis  
75 of an alumina supported copper-cobalt catalyst improved the reducibility of both metal  
76 cations, especially when that fourth element was either Mn or Fe. Alternatively, the  
77 promoter can be deposited over the surface of a as-synthesised alumina before the  
78 deposition of cobalt. In this sense, Park et al. [18] and Park et al. [19], on different  
79 studies, observed that the addition of P to  $\text{Al}_2\text{O}_3$  resulted in the partial formation of  
80  $\text{AlPO}_4$ , which suppressed the formation of  $\text{CoAl}_2\text{O}_4$ . This inhibition effect was also  
81 found for other metallic promoters such as Mg or Zr [20,21]. In all cases, the deposition  
82 of the promoter over the alumina favoured a cobalt-promoter interaction at the cost of a  
83 cobalt-alumina interaction. However, this interaction does not always work in favour of  
84 the redox properties of the cobalt oxide. In this sense, previous investigations on the  
85 effect of surface protection of  $\text{Al}_2\text{O}_3$  with Mg revealed that the resulting Co-Mg  
86 interaction led to the formation of a low reducibility CoO-MgO solid solution, as  
87 reported by Ulla et al. [22] and Ji et al. [23].

88 Considering all the above-mentioned background, and based on our previous results on  
89 the beneficial effect of cerium doping of  $\text{Co}_3\text{O}_4$  bulk catalysts [24], this work proposes  
90 the design of highly active  $\text{Co}/\text{Al}_2\text{O}_3$  catalysts obtained by a previous incorporation of  
91 ceria onto the support prior to cobalt precipitation. The premise supporting this  
92 hypothesis is that the deposited  $\text{CeO}_2$  could have a twofold function as a physical  
93 barrier between cobalt and alumina, thus inhibiting the formation of  $\text{CoAl}_2\text{O}_4$ , and as a  
94 redox promoter for  $\text{Co}_3\text{O}_4$ , thereby enhancing the intrinsic activity of the resulting  
95 catalyst. The specific objective of the study will be to determine the amount of cerium  
96 (5-30%wt.) to be loaded on the alumina support for the optimal performance of a  
97 catalyst with a 30%wt.Co loading in the oxidation of methane in trace amounts (< 1%)  
98 under both dry and humid conditions.

99

## 100 **2. Experimental**

### 101 *2.1. Synthesis of the ceria-alumina supports and cobalt supported catalysts*

102 The ceria-modified alumina supports were prepared by a basic precipitation route of  
103 cerium (III) nitrate hexahydrate ( $\text{Ce}(\text{NO}_3)_3 \cdot 6\text{H}_2\text{O}$ , Sigma Aldrich) on a commercial  $\gamma$ -  
104  $\text{Al}_2\text{O}_3$  (Saint Gobain) thermally stabilized at 850 °C for 8 hours. For each support, 5 g  
105 of  $\gamma$ - $\text{Al}_2\text{O}_3$  were mixed with 100 mL of the cerium precursor with adjusted  
106 concentrations of Ce and then a solution of  $\text{Na}_2\text{CO}_3$  1.2M was added dropwise until the  
107 pH reached 9.5. The temperature was kept constant at 80 °C. The selected cerium  
108 loadings were 5, 10, 15, 20 and 30%wt. After an ageing step of 30 minutes at constant  
109 temperature (80 °C) and pH (9.5), the obtained precipitates were filtered and thoroughly  
110 washed with at least 5 litres of deionised water to remove all residual sodium ions that  
111 could remain in the precursor, which have been proven to inhibit the activity of cobalt  
112 oxide catalysts [25]. These modified supports were denoted as xCe-Al where x stands

113 for the nominal cerium loading. A support of pure ceria ( $\text{CeO}_2$ ) was also synthesised by  
114 the same route starting from a cerium (III) nitrate solution.

115 Cobalt catalysts supported on xCe-Al,  $\text{CeO}_2$  and  $\text{Al}_2\text{O}_3$  were prepared by following the  
116 same synthesis route as for the supports but starting from a mixture of 5 g of each  
117 support (modified alumina, bare ceria and bare alumina, respectively) and 100 mL of a  
118 cobalt (II) nitrate hexahydrate ( $\text{Co}(\text{NO}_3)_2 \cdot 6\text{H}_2\text{O}$ , Fluka) solution. All catalysts were  
119 prepared with a cobalt loading of 30%wt. and denoted as Co/xCe-Al, Co/ $\text{CeO}_2$  and  
120 Co/ $\text{Al}_2\text{O}_3$ , respectively. A reference sample of bulk  $\text{Co}_3\text{O}_4$  was also prepared as well by  
121 precipitation of a solution of cobalt (II) nitrate.

122 All supports and catalytic precursors were dried at 110 °C for 16 hours and then  
123 subjected to calcination in static air to produce the final supports and catalysts. The  
124 calcination protocol was designed on the basis of previous thermogravimetric analysis  
125 (Figure S1, Supplementary Material) and consisted of three heating ramps separated by  
126 30-minute isothermal steps: an initial ramp from room temperature to 125 °C at  
127 5 °C  $\text{min}^{-1}$ , a second ramp up to 300 °C at 1 °C  $\text{min}^{-1}$ , and a final ramp at 5 °C  $\text{min}^{-1}$  up  
128 to 600 °C, temperature that was then maintained for 4 hours.

129

## 130 2.2. *Characterisation techniques*

131 Textural properties were determined from the nitrogen-adsorption isotherms at -196 °C  
132 obtained with a Micromeritics TriStar II apparatus. The specific surface of the samples  
133 was obtained by the BET method, while the pore volume and the pore size distributions  
134 were estimated using the BJH method. All samples were degassed prior to analysis on a  
135 Micromeritics SmartPrep apparatus at 300 °C for 10 hours with a  $\text{N}_2$  flow.

136 The composition was determined by Wavelength Dispersive X-Ray Fluorescence  
137 (WDXRF). From each sample in powder form, a boron glass pearl was prepared by

138 fusion in an induction micro-furnace, by mixing the sample with the flux agent  
139 Spectromelt A12 (Merck) in an approximate proportion of 20:1. Chemical analysis of  
140 each pearl was performed under vacuum, using a PANalytical AXIOS sequential  
141 WDXRF spectrometer, equipped with a Rh tube and three different detectors (gas flow,  
142 scintillation and Xe sealed).

143 Structural properties were determined by X-Ray diffraction, Raman spectroscopy, and  
144 transmission electron microscopy. XRD analysis were performed on a X'PERT-PRO X-  
145 Ray diffractometer using Cu K $\alpha$  radiation ( $\lambda = 1.5406 \text{ \AA}$ ) and a Ni filter. The X-Ray  
146 tube was operated at 40 kV and 40 mA of current. The samples were scanned from an  
147 initial value of  $2\theta = 5^\circ$  to a final value of  $2\theta = 80^\circ$ , with a step size of  $0.026^\circ$  and a  
148 counting time of 2.0 seconds for each step. Phase identification was performed by  
149 comparison of the obtained diffraction patterns with JCPDS (Joint Committee on  
150 Powder Diffraction Standards) database cards. A longer counting time (26.8 s) was  
151 applied to perform a detailed XRD analysis over the xCe-Al supported cobalt catalysts.  
152 The cell size of the cobalt spinel phase was obtained by profile matching of the detailed  
153 XRD patterns using FullProf.2k software. Additionally, the analysis by Raman  
154 spectroscopy was carried out by using a Renishaw InVia Raman spectrometer, coupled  
155 to a Leica DMLM microscope. The excitation wavelength was 514 nm (ion-argon laser,  
156 Modu-Laser). The spatial resolution was 2 microns. For each spectrum 20 seconds were  
157 employed and five scans were accumulated with the 10% of the maximum power of the  
158 514 nm laser in a spectral window of 150-1200  $\text{cm}^{-1}$ .

159 Transmission electron microscopy (TEM) investigations were performed using a Philips  
160 CM200 microscope equipped with LaB<sub>6</sub> crystal as electron source and operating at  
161 200 kV. Bright field images were acquired using a high resolution CCD camera.  
162 HRTEM measurements were carried out with a FEI Titan Cubed G2 60-300 electron



163 microscope at 300 kV equipped with a high-brightness X-FEG Schottky field emission  
164 electron gun and a monochromator and CEOS GmbH spherical aberration (Cs)  
165 corrector on the image side. The images were recorded on a charge-coupled device  
166 (CCD) camera (2kx2k Gatan UltraScan<sup>TM</sup> 1000). X-Ray photoelectron spectroscopy  
167 (XPS) measurements were carried out in a Kratos AXIS Supra spectrometer using a  
168 225 W Al KAl K $\alpha$  radiation source with a pass energy of 160 eV for the general survey  
169 and 20 eV for the specific spectra.

170 Redox properties and Co species distribution was investigated by means of two  
171 temperature-programmed techniques on a Micromeritics Autochem 2920 apparatus.  
172 Temperature-programmed reduction with hydrogen (H<sub>2</sub>-TPR) was performed using a  
173 5% H<sub>2</sub>/Ar mixture as the reducing gas. The analysis protocol involved an initial pre-  
174 treatment step with a 5% O<sub>2</sub>/He mixture at 300 °C for 30 minutes. After cooling down to  
175 room temperature with flowing He, the TPR experiment was performed with a heating  
176 rate of 10 °C min<sup>-1</sup> up to 950 °C for all samples, and that temperature was then  
177 maintained for 10 minutes. The water produced throughout the whole experiment was  
178 eliminated using a cold trap, to avoid interference with the TCD detector. Additional  
179 information regarding the activation of methane was obtained by means of temperature  
180 programmed reaction with a 5% CH<sub>4</sub>/He mixture in the absence of oxygen (CH<sub>4</sub>-TPRe)  
181 coupled to mass spectrometry (MKS Cirrus Quadrupole Mass Spectrometer). The  
182 experiments were carried out up to 600 °C with a heating ramp of 10 °C min<sup>-1</sup> followed  
183 by an isothermal step at 600 °C for 30 minutes.

184

### 185 2.3. *Catalytic activity determination*

186 The activity of the prepared catalysts was tested in a bench-scale fixed bed tubular  
187 reactor (PID Eng&Tech S.L.) in the 200-600 °C temperature range. For each reaction

188 experiment, 1 g of catalysts with a particle size of 0.25-0.3 mm was diluted with 1 g of  
189 inert quartz with a particle size of 0.5-0.8 mm, and the mixture was placed in a  
190 Hastelloy X tube with a K type thermocouple located inside the catalytic bed. The  
191 feedstream composition used was 1%CH<sub>4</sub>, 10%O<sub>2</sub> and N<sub>2</sub> as balance gas, and it was fed  
192 to the reactor with a total flow of 500 mL min<sup>-1</sup>, which accounted for a space velocity of  
193 300 mL CH<sub>4</sub> h<sup>-1</sup> g<sup>-1</sup>. The corresponding gas hourly space velocity calculated as a  
194 function of the total flow rate was approximately 60,000 h<sup>-1</sup>. Additionally, stability tests  
195 were conducted over a prolonged period of time (150 hours) at 450 and 525 °C under  
196 dry and cycling dry/humid (10%vol. H<sub>2</sub>O) conditions. Methane conversion values were  
197 obtained from the methane concentrations measured by a microGC equipped with a  
198 TCD. For each temperature value or reaction time interval, the chromatographic  
199 analysis were performed in triplicate to check the reproducibility. The standard  
200 deviation found was less than 1% in all cases. To ensure that the obtained kinetic results  
201 were not affected by mass or heat transfer limitations, the criteria for intra and extra-  
202 particle heat and mass transfer, and temperature gradients were checked, according to  
203 the Eurokin procedure (Table S1, Supplementary Material).

204

### 205 **3. Results and discussion**

#### 206 *3.1. Characterisation of xCe-Al supports*

207 The composition and textural and structural properties of the ceria-modified alumina  
208 supports were characterised by WDXRF, N<sub>2</sub>-physisorption, XRD and Raman  
209 spectroscopy. Firstly, it should be pointed out that the chemical analysis revealed that  
210 the amount of cerium species deposited on the alumina support was very close to the  
211 nominal loading, namely 5, 10, 15, 20 and 30%wt.Ce (Table 1).

212 The specific surface area, total pore volume and pore size distribution maxima are  
213 summarised in Table 1. The textural properties of the pure oxides ( $\gamma$ -Al<sub>2</sub>O<sub>3</sub> and CeO<sub>2</sub>)  
214 are included for comparative purposes. A roughly linear decrease in surface area was  
215 noticed with increasing Ce content. Thus, this loss was around 25% (with respect to the  
216 bare alumina) for the sample with 30%wt.Ce (139 vs 105 m<sup>2</sup> g<sup>-1</sup>). Judging from these  
217 results the impact of ceria coating was considered moderate. Accordingly, the pore  
218 volume of the samples steadily decreased from 0.56 to 0.32 cm<sup>3</sup> g<sup>-1</sup>.

219 The samples showed type IV isotherms with H2 hysteresis loops, commonly associated  
220 with pore blocking over a wide pore size distribution (Figure S2, Supplementary  
221 material) [26]. No significant change in the hysteresis loops was apparently detected  
222 with the Ce loading. Pore size distribution was estimated according to the BJH method.

223 The samples with low Ce loadings (5-15%wt.) displayed a bimodal distribution peaking  
224 at around 110 and 150 Å, similar to that exhibited by the bare alumina, thus showing  
225 evidence of a good dispersion of the deposited Ce over the surface of the support. For  
226 the 20Ce-Al sample, however, the pore size switched to a unimodal distribution centred  
227 at 110 Å, probably due to the narrowing of the largest pores (150 Å) caused by an  
228 increased cerium deposition. Finally, the 30Ce-Al sample exhibited the same maximum  
229 at 110 Å but with a lower pore volume (0.25 cm<sup>3</sup> g<sup>-1</sup>) compared with the 20Ce-Al  
230 sample (0.30 cm<sup>3</sup> g<sup>-1</sup>). Besides, this sample presented a fraction of small pores with a  
231 maximum around 35 Å derived from a marked pore narrowing of the existing 110 Å  
232 pores because of the massive cerium incorporation.

233 XRD patterns of the xCe-Al supports calcined at 600 °C are shown in Figure 1. This  
234 graph also includes the diffractograms of the bare alumina and bulk ceria. In all cases  
235 the diffraction signals could be indexed as  $\gamma$ -alumina (2 $\theta$  at 37.7, 45.8 and 67.3°, JCPDS  
236 01-074-2206) and cerium oxide (2 $\theta$  at 28.5, 33.3, 47.5, 56.4 and 76.7°, JCPDS 00-004-

237 0593). Note that no peaks attributable to other possible crystalline phases such as  
238 cerium aluminate were noticed. As an additional evidence of the deposition of ceria on  
239 the surface of the alumina support, it was checked that the intensity ratio of the  
240 characteristic signals of CeO<sub>2</sub> (2θ at 47.5°) and Al<sub>2</sub>O<sub>3</sub> (2θ at 45.8°) increased with  
241 cerium loading. Somewhat wide CeO<sub>2</sub> peaks were visible, thereby suggesting that ceria  
242 was present in the form of finely divided particles. An attempt was thus made to  
243 estimate the mean crystallite size of ceria from the peak broadening of the most intense  
244 reflection ((111) plane) using the Scherrer equation. This size was close to 10 nm for the  
245 5Ce-Al, 10Ce-Al and 15Ce-Al samples, and 12 nm for the supports with a higher Ce  
246 content (20Ce-Al and 30Ce-Al samples). These values were in contrast with that found  
247 for the as-prepared bulk ceria (32 nm), thus evidencing a good dispersion of ceria on the  
248 alumina support.

249 TABLE 1

250 FIGURE 1

251 The presence of segregated ceria was further corroborated by Raman spectroscopy.  
252 Thus, all coated alumina supports showed a strong peak assigned to the F<sub>2g</sub> Raman-  
253 active mode characteristic of the fluorite-like lattice of CeO<sub>2</sub> (Figure S3, Supplementary  
254 material). When compared with the Raman spectra of bulk ceria (464 cm<sup>-1</sup>), the signals  
255 were slightly broader and shifted to lower values (462 cm<sup>-1</sup>) due to the alumina-ceria  
256 interaction [27]. Moreover, two additional weak signals at 260 and 595 cm<sup>-1</sup> were  
257 observed. These bands corresponded to nondegenerate longitudinal optical modes of  
258 CeO<sub>2</sub>, which were linked to with oxygen vacancies from partially reduced CeO<sub>2-x</sub>  
259 species [28]. In view of the higher intensity of these features for the 5Ce-Al and 10Ce-  
260 Al supports, the formation of Ce<sup>3+</sup> species, probably in the form of stable CeAlO<sub>3</sub>-like

261 species, was favoured with low Ce loadings. As aforementioned, these species were not  
262 detected by XRD analysis.

263 It seems clear that this varying abundance of  $\text{Ce}^{3+}$  and  $\text{Ce}^{4+}$  as a function of the cerium  
264 content should be consistent with the specific hydrogen uptake of the supports estimated  
265 by  $\text{H}_2$ -TPR. In this way, Figure 2 shows the reduction profiles of bulk ceria and the  
266 various Ce-coated alumina supports. The  $\text{CeO}_2$  sample exhibited a weak signal at 450-  
267 500 °C that corresponded to the surface reduction of the oxide whereas the intense  $\text{H}_2$   
268 uptake peaking at about 800 °C was related to the reduction of the bulk [29]. For the  
269 xCe-Al supports, these two reduction events were also observed. However, while the  
270 surface reduction occurred at 450-500 °C as well, the bulk reduction only required 650-  
271 700 °C, probably due to the relatively small crystallite size of deposited ceria (10-  
272 12 nm). In addition, a small shoulder above 850 °C related to the formation of  $\text{CeAlO}_3$   
273 as a result of the interaction of  $\text{CeO}_2$  and  $\text{Al}_2\text{O}_3$  ( $2\text{CeO}_2 + \text{Al}_2\text{O}_3 + \text{H}_2 \rightarrow 2\text{CeAlO}_3 +$   
274  $\text{H}_2\text{O}$ ) was noted [30]. The generation of this perovskite phase during the reduction  
275 process was further confirmed by subsequent XRD analysis of the samples after the  $\text{H}_2$ -  
276 TPR run. Hence, weak diffraction signals assignable to  $\text{CeAlO}_3$  were visible on all xCe-  
277 Al supports ( $2\theta$  at 23.6, 33.5, 41.4 and 60.1°, JCPDS 00-048-0051) (Figure S4,  
278 Supplementary material). In view of the similar shape of all  $\text{H}_2$ -TPR traces, it could be  
279 assumed the redox characteristics of deposited cerium species, with no marked shift in  
280 the reduction temperatures, remained invariant although the degree of reduction  
281 substantially varied as a function of the cerium loading.

## 282 FIGURE 2

283 The overall  $\text{H}_2$  consumption of the samples expectedly increased with the cerium  
284 content, from 0.09 mmol  $\text{H}_2 \text{ g}^{-1}$  over the 5Ce-Al sample to 0.94 mmol  $\text{H}_2 \text{ g}^{-1}$  over the  
285 30Ce-Al sample (Table 1). However, more notable differences in reducibility were

286 noticed when the specific uptake was examined. Hence, this intrinsic consumption  
287 largely depended on the Ce content of the support (Figure S5, Supplementary material).  
288 Note that this property for the as-synthesised pure bulk CeO<sub>2</sub> was 1.8 mmol H<sub>2</sub> g<sub>Ce</sub><sup>-1</sup>.  
289 The consumption progressively increased from 1.9 mmol H<sub>2</sub> g<sub>Ce</sub><sup>-1</sup> (5Ce-Al) to 3.2-  
290 3.5 mmol H<sub>2</sub> g<sub>Ce</sub><sup>-1</sup> over the 20Ce-Al and 30Ce-Al samples. The low H<sub>2</sub> consumption  
291 observed for the 5Ce-Al and 10Ce-Al supports was coherent with a favoured presence  
292 of Ce<sup>3+</sup> species on these samples, in the form of CeO<sub>2-x</sub> species with a strong interaction  
293 with the alumina, as evidenced by Raman spectroscopy. For higher Ce concentrations,  
294 the predominant cerium species was segregated CeO<sub>2</sub>.

### 295 3.2. Characterisation of Co/xCe-Al catalysts

296 The addition of cobalt oxide (in the 27.2-29.5%wt. range as determined by WDXRF) to  
297 the ceria-modified alumina supports (the actual Ce loading of the catalysts were in the  
298 3.1-18.2%wt. range as determined by WDXRF as well) resulted in a notable, almost  
299 linear loss of surface area of the resulting catalysts (73-102 m<sup>2</sup> g<sup>-1</sup>) (Table 2). With  
300 respect to the corresponding support (105-139 m<sup>2</sup> g<sup>-1</sup>), this accounted for a decline by  
301 20-30%. This negative effect on surface area was comparable to that noticed for the  
302 Co/Al<sub>2</sub>O<sub>3</sub> catalyst (22%). As for the pore volume, the Co/30Ce-Al sample presented the  
303 lowest value (0.25 cm<sup>3</sup> g<sup>-1</sup>) while no significant differences were found among the other  
304 four samples (0.30-0.32 cm<sup>3</sup> g<sup>-1</sup>).

305 TABLE 2

306 The deposition of cobalt species preferentially occurred on the wider pores (150 Å) of  
307 the modified alumina supports with a bimodal pore size distribution, namely 5Ce-Al,  
308 10Ce-Al and 15Ce-Al (Figure S6, Supplementary material). In fact, the profiles of these  
309 catalysts showed a unimodal distribution peaking at 110 Å. In the case of the Co/20Ce-  
310 Al sample the addition of cobalt to this modified support, characterised by a unimodal

311 distribution with a maximum at 110 Å, resulted in a shift of the pore size distribution to  
312 slightly lower values (around 90 Å). This shift was not observed over the Co/30Ce-Al  
313 catalyst with respect to its counterpart alumina support (30Ce-Al), thus suggesting that  
314 cobalt oxide was partially present on the external surface of this sample.

315 Figure 3 shows the diffractograms of the Co/xCe-Al catalysts. For comparative  
316 purposes, the patterns of the Co/Al<sub>2</sub>O<sub>3</sub> and Co/CeO<sub>2</sub> samples were included as well.  
317 Along with the characteristic features of the ceria phase ( $2\theta = 28.5, 33.3, 47.5, 56.4$  and  
318  $76.7^\circ$ ), a set of signals at  $2\theta = 31.3, 37.0, 45.1, 59.4$  and  $65.3^\circ$  were clearly  
319 distinguished. These were related to a spinel-like cobalt phase, namely Co<sub>3</sub>O<sub>4</sub> (JCPDS  
320 00-042-1467) and/or CoAl<sub>2</sub>O<sub>4</sub> (JCPDS 00-044-0160). The formation of cobalt  
321 aluminate was plausible due to the interaction of Co<sub>3</sub>O<sub>4</sub> and Al<sub>2</sub>O<sub>3</sub> at high temperatures  
322 [31]. Unfortunately, it was not possible to differentiate between these two oxides since  
323 both phases crystallise in the cubic structure. Obviously, the formation of CoAl<sub>2</sub>O<sub>4</sub> was  
324 only ruled out in the case of the 30Co/CeO<sub>2</sub> sample. After the addition of cobalt the  
325 crystallite size of CeO<sub>2</sub>, which was in 9-14 nm range, was not appreciably modified  
326 when compared with the corresponding xCe/Al support (10-12 nm). As for the size of  
327 the spinel-like cobalt phase estimated from the peak broadening of the signal at  $37.1^\circ$ , it  
328 remained almost constant (23-24 nm) irrespective of the composition of the support.  
329 Only for the Co/30Ce-Al catalyst the size was considerably larger (31 nm), probably  
330 due to the high cerium loading.

### 331 FIGURE 3

332 The Raman spectra of the cobalt catalysts supported on pure alumina (Co/Al<sub>2</sub>O<sub>3</sub>), pure  
333 ceria (Co/CeO<sub>2</sub>) and ceria/alumina (Co/xCe-Al) are included in Figure 4. As a  
334 reference, the spectrum of pure Co<sub>3</sub>O<sub>4</sub> is shown as well. Apart from a relatively weak  
335 band at  $462\text{ cm}^{-1}$  (F<sub>2g</sub> mode of CeO<sub>2</sub>), all supported catalysts displayed the five Raman

336 actives modes associated with  $\text{Co}_3\text{O}_4$ , namely three  $\text{F}_{2g}$  modes located at 194, 519 and  
337  $617\text{ cm}^{-1}$ , and the  $\text{E}_g$  and  $\text{A}_{1g}$  modes at 479 and  $687\text{ cm}^{-1}$ , respectively [32,33]. Except  
338 from the  $\text{Co}/\text{CeO}_2$  catalyst, two shoulders at 705 and  $725\text{ cm}^{-1}$  attached to the  $\text{A}_{1g}$   
339 vibration mode were visible. These two signals suggested the presence of cobalt  
340 aluminate [34,35]. It was found out that the intensity of these features was more notable  
341 over the  $\text{Co}/\text{Al}_2\text{O}_3$  and  $\text{Co}/5\text{Ce-Al}$  samples, and tended to decrease when ceria was  
342 deposited with a higher loading ( $>10\%\text{wt.Ce}$ , more significantly for  $30\%\text{wt.Ce}$ ).  
343 Although the formation of this undesired cobalt phase was not completely inhibited, it  
344 seemed that incorporated ceria acted as an efficient physical barrier to prevent the  
345 reaction between  $\text{Co}_3\text{O}_4$  and  $\text{Al}_2\text{O}_3$  to some extent. From a catalytic point of view, the  
346 ceria coating of the alumina support would favour an increase in the amount of highly  
347 active  $\text{Co}_3\text{O}_4$  at the cost of  $\text{CoAl}_2\text{O}_4$ .

#### 348 FIGURE 4

349 A closer inspection of the dependence of the  $\text{A}_{1g}$  mode with the Ce content of the  
350 catalysts could be helpful in determining a possible distortion of the  $\text{Co}_3\text{O}_4$  lattice due to  
351 the partial insertion of cerium cations. This effect was analysed in terms of the shift and  
352 the full width at half maximum (FWHM) of this signal (Figure S7, Supplementary  
353 material). On one hand, it was observed that the location of the band varied from  
354  $689\text{ cm}^{-1}$  in the  $\text{Co}/\text{Al}_2\text{O}_3$  and bulk  $\text{Co}_3\text{O}_4$  samples to  $681\text{ cm}^{-1}$  in the  $\text{Co}/\text{CeO}_2$  sample,  
355 thus pointing out that the lattice of  $\text{Co}_3\text{O}_4$  was much more affected by the presence of  
356  $\text{CeO}_2$ . As the Ce/Co molar ratio of the  $\text{Co}/x\text{Ce-Al}$  catalysts increased the band  
357 progressively shifted to lower values, from  $689\text{ cm}^{-1}$  for  $\text{Co}/\text{Al}_2\text{O}_3$  to  $688\text{-}685\text{ cm}^{-1}$  for  
358  $\text{Co}/5\text{Ce-Al}$ ,  $\text{Co}/10\text{Ce-Al}$  and  $\text{Co}/15\text{Ce-Al}$ , and to  $682\text{-}680\text{ cm}^{-1}$  for  $\text{Co}/20\text{Ce-Al}$ ,  
359  $\text{Co}/30\text{Ce-Al}$  and  $\text{Co}/\text{CeO}_2$ . It should be noticed that the other Raman active modes ( $\text{F}_{2g}$   
360 and  $\text{E}_g$ ) shifted as well. This redshift of the  $\text{Co}_3\text{O}_4$  signals could be attributed to the



361 distortion of the spinel lattice, possibly due to insertion of Ce ions [36]. Consistently,  
362 the FWHM values of this band were higher for the Ce-rich cobalt catalysts (25-26 cm<sup>-1</sup>  
363 compared with 14-19 cm<sup>-1</sup> for Co/5Ce-Al, Co/10Ce-Al and Co/15Ce-Al).

364 The structural change of the Co<sub>3</sub>O<sub>4</sub> lattice was further confirmed by the estimation of  
365 the cell parameter of the Co spinel from XRD patterns. As aforementioned, the detected  
366 diffraction signals could be assigned to both Co<sub>3</sub>O<sub>4</sub> and CoAl<sub>2</sub>O<sub>4</sub>. Consequently, the  
367 position shifts that denote the change in the cell size could be initially attributed to  
368 distortion of both phases. However, since only the Raman vibration modes of Co<sub>3</sub>O<sub>4</sub>  
369 phase (and not those of CoAl<sub>2</sub>O<sub>4</sub> phase) evidenced changes with the addition of Ce, the  
370 shift in the diffraction signals was assumed to occur only due to distortion of the cobalt  
371 oxide phase. Thus, the cell size of Co<sub>3</sub>O<sub>4</sub> in the Co/xCe-Al catalysts was found to be  
372 larger than that of the catalyst supported over bare alumina (8.077 Å), as shown in  
373 Figure S8 (Supplementary material). More importantly, for the Co/20Ce-Al and  
374 Co/30Ce-Al samples, the cell size displayed a maximum value (8.092 Å), which  
375 evidenced the largest lattice distortion, in accord with the results obtained from Raman  
376 spectroscopy. The enlargement of the unit cell of Co<sub>3</sub>O<sub>4</sub> has been previously reported  
377 by other authors [37,38] and is associated with the larger ionic radius of Ce<sup>4+</sup> ions  
378 (101 pm), with respect to Co<sup>2+</sup> and Co<sup>3+</sup> ions (79 and 69 pm, respectively). Note that  
379 this eventual insertion of Ce<sup>4+</sup> ions into the spinel lattice would be accompanied by an  
380 increase in the amount of Co<sup>3+</sup> so as to maintain the charge balance [39].

381 HAADF-STEM images along with the corresponding EDX maps of the Co/xCe-Al  
382 catalysts are shown in Figure 5. This analysis evidenced that cobalt species were indeed  
383 located on the surface of the ceria-modified alumina with a low presence of segregated  
384 entities. In addition, it was noteworthy that some regions of the support were not  
385 massively covered by cobalt. The spinel active phase was present as crystallites with

386 average sizes around 20-25 nm, which was in good agreement with XRD results  
387 (Table 2), that tended to aggregate into larger patches of 100-150 nm. Only for the  
388 Co/30Ce-Al sample, segregated  $\text{Co}_3\text{O}_4$  crystallites with sizes up to 50-60 nm were  
389 marginally observed. As for the cerium, it was homogeneously distributed on the  
390 support in the form of quite small crystallites (smaller than 5 nm). Additionally,  $\text{CeO}_2$   
391 clusters of about 10 nm were also detected, in line with XRD results (Table 2). For the  
392 Co/30Ce-Al sample, the size of the clusters increased up to 20 nm, as also evidenced by  
393 XRD analysis.

394 Finally, Figure S9 (Supplementary material) shows some selected HRTEM images,  
395 where the lattice fringes of  $\text{Co}_3\text{O}_4$  and  $\text{CeO}_2$  could be resolved, along with their  
396 corresponding Fast Fourier Transform (FFT) spot patterns. For the cobalt spinel, two  
397 lattice spaces, namely 0.29 and 0.24 nm, were identified, which corresponded to the  
398  $\{220\}$  and the  $\{311\}$  planes, respectively. On the other hand, for the ceria two lattice  
399 spaces of 0.31 and 0.27 nm were observed, which corresponded to the  $\{111\}$  and  $\{200\}$   
400 planes, respectively.

#### 401 FIGURE 5

402 The surface structure and composition was investigated by XPS. The distribution of  
403 cobalt and oxygen species was determined from the  $\text{Co}2\text{p}$  and  $\text{O}1\text{s}$  spectra of the  
404 samples, respectively (Figure S10, Supplementary material). In particular, the  $\text{Co } 2\text{p}_{3/2}$   
405 signal could be deconvoluted in five different contributions. The two signals located at  
406 lower binding energies, namely 779.5 and 780.7 eV, were attributed to the presence of  
407  $\text{Co}^{3+}$  and  $\text{Co}^{2+}$  cations in a spinel phase, respectively, while the signal centred at about  
408 782.3 eV was attributed to the presence of  $\text{CoO}$  species [40]. The presence of this oxide  
409 was comparable on all samples, and it accounted for around 5-8% of the total detected  
410 signal. Finally, the two signals located at higher binding energies (785.5 and 789.5 eV)

411 were identified as the satellite signals from  $\text{Co}^{2+}$  and  $\text{Co}^{3+}$  ions, respectively [41]. On  
412 the other hand, the O 1s spectra showed three different signals located at 529.8, 530.8  
413 and 532.4 eV, respectively. The first signal was assigned to oxygen species from the  
414 spinel lattice ( $\text{O}_{\text{latt}}$ ), the second one was related to weakly adsorbed oxygen species on  
415 the surface ( $\text{O}_{\text{ads}}$ ) and the last feature was attributed to the presence of hydroxyl groups  
416 from adsorbed water [42].

417 Table 3 includes the surface molar composition of the investigated catalysts. The bulk  
418 composition as determined by WDXRF is also included for comparative purposes.  
419 Initially the properties of the reference supported catalysts, namely  $\text{Co}/\text{Al}_2\text{O}_3$  and  
420  $\text{Co}/\text{CeO}_2$  samples, will be discussed. The  $\text{Co}/\text{Al}_2\text{O}_3$  sample showed a surface  $\text{Co}^{3+}/\text{Co}^{2+}$   
421 molar ratio of 0.67, which was noticeably lower compared with that of the  $\text{Co}/\text{CeO}_2$   
422 catalyst (0.95). Taking the latter value as representative of the supported  $\text{Co}_3\text{O}_4$  oxide  
423 phase, the low value of the alumina-supported catalyst was in agreement with the  
424 significant presence of  $\text{CoAl}_2\text{O}_4$ , where cobalt cations are in the +2 oxidation state, as  
425 suggested by Raman spectroscopy. As the formation of cobalt aluminate involves a  
426 gradual diffusion of Co cations into the alumina structure, this necessarily resulted in a  
427 lower presence of cobalt on the surface, with a Co/Al molar ratio of 0.32. Furthermore,  
428 the relative abundance of surface cobalt increased for the Ce-containing samples as  
429 revealed by their higher  $\text{Co}/(\text{Ce}+\text{Al})$  molar ratios (up to 0.84 for the  $\text{Co}/20\text{Ce}-\text{Al}$   
430 sample). This finding was coherent with a less favoured formation of cobalt aluminate  
431 due to the barrier effect of ceria, in line with the results derived from Raman  
432 spectroscopy.

433 TABLE 3

434 On the other hand, the  $\text{Co}^{3+}/\text{Co}^{2+}$  molar ratio of the  $\text{Co}/x\text{Ce}-\text{Al}$  catalysts, except for the  
435  $\text{Co}/5\text{Ce}-\text{Al}$  sample), was higher (0.99-1.38) than that of the  $\text{Co}/\text{CeO}_2$  catalyst. This fact

436 revealed that some cerium cations were likely incorporated into the  $\text{Co}_3\text{O}_4$  lattice, as  
437 previously suggested by XRD. This partial insertion necessarily implied an increase in  
438 the abundance of  $\text{Co}^{3+}$  cations at the cost of  $\text{Co}^{2+}$  cations to maintain the charge balance.  
439 This higher abundance of  $\text{Co}^{3+}$  species on the surface of the samples with increasing Ce  
440 loading was accompanied by a concomitant more notable presence of lattice oxygen  
441 species in the Co/xCe-Al catalysts (Table 3). These type of oxygen species are usually  
442 involved in the oxidation of methane by a Mars–van Krevelen mechanism. As shown in  
443 Figure 6, the relative presence of both species increased with cerium loading and was  
444 optimised for the Co/20Ce-Al catalyst.

#### 445 FIGURE 6

446 The nature of deposited cobalt species and their interaction with underlying ceria-coated  
447 alumina was examined by  $\text{H}_2$ -TPR analysis (Table 4). Initially the behaviour of cobalt  
448 catalysts supported on pure alumina or ceria ( $\text{Co}/\text{Al}_2\text{O}_3$  and  $\text{Co}/\text{CeO}_2$ , respectively) was  
449 compared. Besides, the reduction profile of bulk ceria was taken into consideration  
450 (Figure S11, Supplementary material). Both cobalt catalysts displayed a notable  $\text{H}_2$   
451 uptake between 200-600 °C that was related to the reduction of precipitated  $\text{Co}_3\text{O}_4$ . This  
452 contribution showed two more or less discernible peaks at 310 and 380 °C, which were  
453 indicative of the sequential reduction to CoO and metallic Co, respectively [32,43].  
454 Except for a small band observed at 800 °C (this peak corresponded to the reduction of  
455 ceria support), the  $\text{Co}/\text{CeO}_2$  catalyst did not consume hydrogen between 600-800 °C.  
456 The overall  $\text{H}_2$  uptake was  $7.6 \text{ mmol H}_2 \text{ g}^{-1}$ . Interestingly, it was found that when  
457 subtracting the amount of  $\text{H}_2$  theoretically required for full reduction of deposited  
458  $\text{Co}_3\text{O}_4$  (equivalent to  $22.6 \text{ mmol H}_2 \text{ g}_{\text{Co}}^{-1}$ , according to following the equation  
459  $\text{Co}_3\text{O}_4 + 4\text{H}_2 \rightarrow 3\text{Co} + 4\text{H}_2\text{O}$ ) from the overall  $\text{H}_2$  consumption of the sample, the  $\text{H}_2$   
460 consumption related to the reduction of the support could be estimated. This value was

461 1.8 mmol H<sub>2</sub> g<sub>Ce</sub><sup>-1</sup>, that coincided with the specific consumption measured for the pure  
462 CeO<sub>2</sub> support. These results led us to conclude that no mutual effects on the reducibility  
463 of both cobalt oxide and ceria existed for this catalyst.

464 In the case of Co/Al<sub>2</sub>O<sub>3</sub>, an additional peak between 550-750 °C was clearly  
465 ascertained. This was assigned to the presence of significant quantities of CoAl<sub>2</sub>O<sub>4</sub>  
466 derived from the strong interaction between Co<sub>3</sub>O<sub>4</sub> and Al<sub>2</sub>O<sub>3</sub>, as also evidenced by  
467 Raman spectroscopy. In fact, the total measured amount of H<sub>2</sub> (5.6 mmol H<sub>2</sub> g<sup>-1</sup>) was  
468 rather far from the stoichiometric uptake (6.8 mmol H<sub>2</sub> g<sup>-1</sup>) when assuming that the  
469 cobalt phase was exclusively Co<sub>3</sub>O<sub>4</sub>. These findings led to the conclusion that the  
470 reducibility of free Co<sub>3</sub>O<sub>4</sub> (cobalt species whose reduction occurred at 200-600 °C) was  
471 much more favoured when cobalt was deposited over ceria instead of alumina, although  
472 the interaction between cobalt and ceria did not seem to enhance the redox properties of  
473 the Co<sub>3</sub>O<sub>4</sub> deposited over pure ceria in comparison with pure Co<sub>3</sub>O<sub>4</sub>. Simultaneously,  
474 the reducibility of ceria was also not improved.

#### 475 TABLE 4

476 The H<sub>2</sub>-TPR profiles of the cobalt catalysts supported on ceria-alumina also consisted of  
477 two H<sub>2</sub> uptakes at 200-550 °C and 550-800 °C (Figure 7). The total H<sub>2</sub> consumption of  
478 the samples is given in Table 4. In all cases the H<sub>2</sub> uptake was larger than that shown by  
479 the Co/Al<sub>2</sub>O<sub>3</sub> sample. A significant increase by 5-16% was found with the amount of  
480 cerium in the support. Above 15%wt.Ce the consumption was rather similar (6.5-  
481 6.7 mmol H<sub>2</sub> g<sup>-1</sup>). While no significant changes in the reduction onset temperature  
482 (about 250 °C) were observed, the relative contribution of these reduction events  
483 seemed to be shifted in favour of the low-temperature band with the Ce loading  
484 (Table 4). The observed increase in the H<sub>2</sub> uptake at low temperature could be  
485 rationalised in terms of a favoured reduction of Co<sub>3</sub>O<sub>4</sub> with a distorted lattice due to

486 cerium doping as revealed by XRD and XPS analysis. Another plausible phenomenon  
487 that would contribute to a higher reducibility between 200 and 500 °C could be a larger  
488 extent of ceria reduction owing to the transfer of hydrogen by metallic cobalt onto the  
489 ceria surface [44,45]. On the other hand, and in agreement with Raman spectroscopy,  
490 the interaction between  $\text{Co}_3\text{O}_4$  and  $\text{Al}_2\text{O}_3$  to give  $\text{CoAl}_2\text{O}_4$  was somewhat inhibited by  
491 deposited ceria, thereby resulting in a decreased  $\text{H}_2$  uptake at high temperatures.

492 In sum, the presence of ceria deposited on the alumina surface resulted in remarkable  
493 changes in the redox properties by distorting the  $\text{Co}_3\text{O}_4$  crystalline lattice and/or  
494 promoting the ceria reducibility and/or inhibiting the formation of  $\text{CoAl}_2\text{O}_4$ . These  
495 positive effects eventually led to a larger abundance of highly active oxygen, in the  
496 form of lattice oxygen species as evidenced by XPS analysis, over the Co/xCe-Al  
497 catalysts in comparison with the Co/ $\text{Al}_2\text{O}_3$  counterpart.

#### 498 FIGURE 7

499 More useful insights on the influence of the catalyst composition on the reactivity of  
500 available oxygen species for methane oxidation were obtained by  $\text{CH}_4$ -TPRe analysis  
501 coupled to mass spectrometry. The analysis was performed between 50 and 600 °C with  
502 a subsequent isothermal step at this temperature for 30 minutes. The evolution of  $\text{CO}_2$   
503 ( $m/z = 44$ ) and  $\text{CO}$  ( $m/z = 28$ ) was monitored (Figure 8).  $\text{CO}_2$  formation occurred at two  
504 clearly distinct temperature windows, namely 425-500 °C (only  $\text{CO}_2$  was detected) and  
505 above 580 °C (both  $\text{CO}$  and  $\text{CO}_2$  were detected accompanied by  $\text{H}_2$  as well, not shown  
506 in Figure 8). In the low temperature range both Co/ $\text{Al}_2\text{O}_3$  and Co/ $\text{CeO}_2$  catalysts led to  
507 the generation of  $\text{CO}_2$  at about 485 °C, which was attributed to the oxidation of methane  
508 by oxygen species associated with  $\text{Co}^{3+}$  ions. Table 4 includes the  $\text{O}_2$  consumption  
509 corresponding to this generation of  $\text{CO}_2$  for all examined catalysts. Note that the lowest  
510 value ( $0.28 \text{ mmol O}_2 \text{ g}_{\text{Co}}^{-1}$ ) corresponded to the Co/ $\text{Al}_2\text{O}_3$  sample in agreement with the

511 marked presence of  $\text{CoAl}_2\text{O}_4$ . When cerium was added to the alumina support, the  $\text{CO}_2$   
512 formation was more evident and took place at significantly lower temperatures. Figure 6  
513 revealed that the extent of  $\text{CH}_4$  oxidation was noticeably favoured with the presence of  
514 lattice oxygen species. On the other hand, the reduction process interestingly occurred at  
515  $465\text{ }^\circ\text{C}$  over the Co/20Ce-Al sample and consumed the largest amount of oxygen  
516 ( $0.88\text{ mmol O}_2\text{ g}_{\text{Co}}^{-1}$ ). Moreover, the temperature of the onset of reduction (marked by  
517 arrows in Figure 8) was significantly lower for the Co/20Ce-Al and Co/30Ce-Al  
518 samples (around  $350\text{ }^\circ\text{C}$ ) in comparison with the rest of the samples (around  $400\text{ }^\circ\text{C}$ ).  
519 As stated above, the generation of  $\text{CO}_2$  was also visible at higher temperatures owing to  
520 the oxidation of methane by oxygen species associated with  $\text{Co}^{2+}$  ions [46]. This mass  
521 signal was detected at  $600\text{ }^\circ\text{C}$  during the isothermal period. Exceptionally,  $\text{CO}_2$  was  
522 detected at  $580\text{ }^\circ\text{C}$  over the Co/20Ce-Al catalyst, thereby suggesting a higher mobility  
523 of the oxygen species in this sample. In all cases, the high-temperature oxidation was  
524 accompanied by the generation of  $\text{CO}$  and  $\text{H}_2$  to some extent that could be due to partial  
525 oxidation or cracking of methane in the presence of metallic or oxygen-deficient cobalt  
526 species [47]. In fact, the diffraction pattern of the samples after the  $\text{CH}_4$ -TPRe run  
527 evidenced the formation of graphitic carbon (signal at  $2\theta = 26.6^\circ$ ) due to the occurrence  
528 of these two reactions [48].

529 **FIGURE 8**

530

### 531 3.3. *Catalytic behaviour of Co/xCe-Al catalysts*

532 The performance of the synthesised cobalt catalysts was examined by their  
533 corresponding light-off curves at  $300\text{ mL CH}_4\text{ g}^{-1}\text{ h}^{-1}$  ( $30000\text{ mL g}^{-1}\text{ h}^{-1}$ ) in the 200-  
534  $600\text{ }^\circ\text{C}$  temperature range (Figure 9). Each catalyst was subjected to at least three  
535 consecutive runs. It was found that the corresponding light-off curves were all

536 comparable after the second cycle. The representative light-off curve of each catalyst  
537 corresponded to the third consecutive run. For the sake of comparison the conversion-  
538 temperature profiles of the Co/Al<sub>2</sub>O<sub>3</sub>, Co/CeO<sub>2</sub> and bulk CeO<sub>2</sub> catalysts are also  
539 included. It must be noticed that all catalysts exhibited a 100% selectivity towards CO<sub>2</sub>,  
540 irrespective of their cerium loading. While a negligible activity in the whole  
541 temperature range was noticed for bare ceria, the cobalt catalyst supported over  
542 uncoated alumina (Co/Al<sub>2</sub>O<sub>3</sub>) gave a T<sub>50</sub> value at around 550 °C. However, this sample  
543 did not achieve a 100% conversion at the highest investigated temperature (only around  
544 80% at 600 °C). Interestingly, all Co/xCe-Al catalysts evidenced a better behaviour  
545 irrespectively the ceria loading, with T<sub>50</sub> values in the 480-540 °C temperature range  
546 and a conversion higher than 95% at 600 °C. On the other hand, the observed higher  
547 efficiency of the Co/CeO<sub>2</sub> sample (T<sub>50</sub> of 500 °C) with respect to its counterpart  
548 supported on pure alumina indicated that a cobalt-ceria interaction was catalytically  
549 more preferable. The following overall trend was found: Co/20Ce-Al (480 °C) >  
550 Co/15Ce-Al (490 °C) > Co/30Ce-Al (495 °C) > Co/CeO<sub>2</sub> ≈ Co/10Ce-Al (505 °C) >  
551 Co/5Ce-Al (525 °C) > Ce-Al<sub>2</sub>O<sub>3</sub> (550 °C). Thus, an optimum cerium loading (20% wt.)  
552 deposited on alumina was defined.

553 **FIGURE 9**

554 A clearer evidence of the superior performance of the Co/20Ce-Al catalyst was given by  
555 the analysis of the specific reaction rate shown by each Co/xCe-Al sample (Figure 10).  
556 This reaction rate was calculated under differential conditions (conversion <15%) at  
557 400 °C. A volcano-type relationship was distinctly seen, given that the reaction rate  
558 progressively increased with Ce loading between 0 and 20%wt. (as referred to the  
559 alumina support) from 1.2 to 3.3 mmol<sub>CH<sub>4</sub></sub> g<sub>Co</sub><sup>-1</sup> h<sup>-1</sup>, to then decrease significantly for the  
560 samples with a higher Ce concentration (2.9 mmol<sub>CH<sub>4</sub></sub> g<sub>Co</sub><sup>-1</sup> h<sup>-1</sup>). This trend was also



561 consistent with the intrinsic activity shown by the cobalt catalyst supported on pure  
562 ceria ( $2.1 \text{ mmol}_{\text{CH}_4} \text{ g}_{\text{Co}}^{-1} \text{ h}^{-1}$ ). The results evidenced a promoted activity of  $\text{Co}_3\text{O}_4$  when  
563 supported on ceria-coated alumina. The positive effect of ceria coating was mainly  
564 ascribed to the enhanced reactivity of the oxygen species of  $\text{Co}_3\text{O}_4$  as also shown in  
565 Figure 10. Hence, a marked dependence of the intrinsic activity with the amount of  $\text{O}_2$   
566 consumed at low temperatures ( $< 500 \text{ }^\circ\text{C}$ ) in the  $\text{CH}_4$ -TPRe runs was evidenced. As  
567 aforementioned, ceria addition was useful for partially reducing the amount of inactive  
568  $\text{CoAl}_2\text{O}_4$  and simultaneously inducing a distortion of the structure of  $\text{Co}_3\text{O}_4$ . Both  
569 phenomena ultimately led to catalysts with an enhanced oxidation ability. The apparent  
570 activation energy of the reaction over the investigated cobalt catalysts was evaluated by  
571 applying the integral method. A first pseudo-order for methane and a zero pseudo-order  
572 for oxygen were assumed on the basis of a simplified Mars–van Krevelen kinetics for  
573 this reaction studied with a high  $\text{O}_2/\text{CH}_4$  molar ratio [49,50]. The corresponding plots  
574 for the linearized kinetic equation of the integral reactor are shown in Figure S12,  
575 Supplementary material. The values for the apparent activation energy were in the 80-  
576  $83 \text{ kJ mol}^{-1}$  range for all catalysts, which were coherent with the value obtained with a  
577 bulk  $\text{Co}_3\text{O}_4$  catalyst ( $78 \text{ kJ mol}^{-1}$ ) [24].

578 **FIGURE 10**

579 Finally, the stability of the most active sample (Co/20Ce-Al) was examined under two  
580 different scenarios. On one hand, the evolution of conversion with time on stream of a  
581 fresh sample was followed at  $450 \text{ }^\circ\text{C}$  for 60 hours. Then, the reaction temperature was  
582 increased up to  $525 \text{ }^\circ\text{C}$  and the sample was maintained at this temperature during  
583 additional 90 hours. Results from this experiment carried out under dry conditions are  
584 shown in Figure 11. A relatively constant conversion level around 30% was observed at  
585  $450 \text{ }^\circ\text{C}$  with no clear evidences of deactivation. After raising the temperature at  $525 \text{ }^\circ\text{C}$ ,

586 a progressive loss of conversion from 78% to 64% (25 hours), and to 58% (25 hours)  
587 was noticed. Then, conversion remained stable for the remaining 40 hours of the  
588 stability test.

589 In a second scenario a fresh sample was also evaluated during a prolonged time span  
590 (150 hours), in the absence or presence of water (10%) in the feed stream. Figure 11  
591 includes the evolution of methane conversion during the stability test, where dry and  
592 humid conditions were cycled each 25 hours at constant temperature (525 °C). The  
593 results revealed a significant deactivation for the first 25 hours under dry conditions,  
594 with a conversion decrease from 80 to 64%. Note that the conversion profile for this  
595 time interval was virtually identical to that observed for the same conditions used in the  
596 first stability test. When water was added to the gas stream, the impact on conversion  
597 was considerable as conversion fell down to about 30%. When dry conditions were re-  
598 established, methane conversion was partially recovered to give a stable value close to  
599 52%. However, this was a little bit far from 58% dictated by the run carried out under  
600 exclusively dry conditions. Once again, the admission of water led to an inhibition of  
601 activity as conversion was 25%. When water admission was stopped, conversion again  
602 increased (up to 48%), and finally decreased down to around 20% in the presence of  
603 water. These results evidenced that the suggested inhibiting effect of water was not only  
604 due to competition effects with methane for surface adsorption but it was also affecting  
605 the physico-chemical properties of the catalyst [51,52].

606

#### FIGURE 11

607 The used samples from the two long-term stability tests conducted under dry and  
608 dry/humid conditions, namely Co/20Ce-Al(d) and Co/20Ce-Al(d/h) samples, were  
609 characterised by N<sub>2</sub> physisorption, XRD and CH<sub>4</sub>-TPRe. Attention was paid on the  
610 eventual changes on the surface area, the crystallite size of oxide phases and the amount

611 of active oxygen species at low temperatures (<550 °C). It was found that the  
612 composition of the feed stream clearly affected the physico-chemical properties of the  
613 sample (Table S2, Supplementary material). Thus, a decrease in the surface area was  
614 observed (from 93 to 85 m<sup>2</sup> g<sup>-1</sup> over Co/20Ce-Al(d)), which was slightly larger  
615 (79 m<sup>2</sup> g<sup>-1</sup>) when the sample operated in the presence of large amounts of steam.  
616 However, both deposited ceria and cobalt spinel phase exhibited a high thermal stability  
617 in view of their relatively invariable crystallite size (12 and 23 nm, respectively). The  
618 negative impact of water was reflected in the amount and reactivity of active oxygen  
619 species as estimated by CH<sub>4</sub>-TPRe analysis. The corresponding profiles are included in  
620 Figure S13, Supplementary material and revealed that the O<sub>2</sub> consumption at low  
621 temperatures decreased by 4% for the Co/20Ce-Al(d) sample and 16% for the Co/20Ce-  
622 Al(d/h) sample. Moreover, a concomitant shift of the peak temperatures for this uptake  
623 was noticed from 465 to 470 °C over the Co/20Ce-Al(d) sample and 480 °C over the  
624 Co/20Ce-Al(d/h) sample.

625

## 626 **Conclusions**

627 The effect of cerium deposition on alumina-supported cobalt oxide catalysts for the  
628 complete oxidation of lean methane was studied. The addition of cerium (5-30% wt.) to  
629 the alumina was carried out prior to the deposition of cobalt (30% wt.) by a precipitation  
630 synthesis route. The textural properties of the modified supports were hardly modified  
631 with respect to those of bare alumina, due to the good dispersion of ceria over the  
632 surface of the alumina. This dispersion also was responsible for a relatively strong  
633 interaction between alumina and deposited ceria that resulted in an increased Ce<sup>3+</sup>  
634 content, especially at low Ce loadings (5-15% wt.). For higher Ce loadings (20-30% wt.)

635 the cerium-alumina interaction was weaker, thus resulting in a deposited ceria with a  
636 higher  $Ce^{4+}$  content and better reducibility with respect to pure bulk ceria.  
637 When cobalt was deposited over the modified supports, a dual effect of ceria was  
638 evidenced. On one hand, ceria was found to act as a physical barrier between alumina  
639 and deposited cobalt, reducing the cobalt-alumina interaction and the subsequent cobalt  
640 aluminate formation, more remarkably with higher Ce loadings (20-30% wt.). On the  
641 other hand, the interaction between cobalt and ceria led to a partial incorporation of  
642 cerium ions into the structure of the cobalt oxide. Both findings ultimately led to a  
643 larger abundance of  $Co^{3+}$  and therefore to a promoted mobility of the lattice oxygen  
644 species with ceria loading. Consequently, cobalt catalysts supported over ceria-alumina  
645 were significantly more active than that supported over bare alumina. The best  
646 behaviour was found for the Co/20Ce-Al sample. Furthermore, this sample exhibited a  
647 relatively good thermal stability for prolonged reaction time intervals (150 h) under dry  
648 conditions. However, the presence of water vapour markedly affected the catalytic  
649 performance although this negative effect was partially reversible.

650

## 651 **Acknowledgements**

652 The author wish to thank the financial support provided by the Ministry of Economy  
653 and Competitiveness (CTQ2016-80253-R AEI/FEDER, UE), Basque Government  
654 (IT1297-19) and the University of the Basque Country UPV/EHU (PIF15/335), and the  
655 technical and human support provided by SGIker (UPV/EHU).

656

## 657 **Appendix A. Supplementary data**

658 Supplementary data associated with this article can be found in the online version.

659

660 **References**

- 661 [1] G. Zhai, J. Wang, Z. Chen, W. An, Y. Men, *Chem. Eng. J.* 337 (2018) 488-498.  
662 <https://doi.org/10.1016/j.cej.2017.12.141>.
- 663 [2] B. Bai, H. Arandiyani, J. Li, *Appl. Catal. B Environ.* 142-143 (2013) 677-683.  
664 <https://doi.org/10.1016/j.apcatb.2013.05.056>.
- 665 [3] G. Ercolino, P. Stelmachowski, G. Grzybek, A. Kotarba, S. Specchia, *Appl. Catal.*  
666 *B Environ.* 206 (2017) 712-725. <https://doi.org/10.1016/j.apcatb.2017.01.055>.
- 667 [4] K. Lehtoranta, T. Murtonen, H. Vesala, P. Koponen, J. Alanen, P. Simonen, T.  
668 Rönkkö, H. Timonen, S. Saarikoski, T. Maunula, K. Kallinen, S. Korhonen,  
669 *Emiss. Control Sci. Technol.* 3 (2017) 142-152. [https://doi.org/10.1007/s40825-](https://doi.org/10.1007/s40825-016-0057-8)  
670 [016-0057-8](https://doi.org/10.1007/s40825-016-0057-8).
- 671 [5] M. Keenan, R. Pickett, E. Tronconi, I. Nova, N. Kinnunen, M. Suvanto, T.  
672 Maunula, K. Kallinen, R. Baert, *Top. Catal.* 62 (2019) 273-281.  
673 <https://doi.org/10.1007/s11244-018-1127-7>.
- 674 [6] J. Chen, H. Arandiyani, X. Gao, J. Li, *Catal. Surv. Asia* 19 (2015) 140-171.  
675 <https://doi.org/10.1007/s10563-015-9191-5>.
- 676 [7] F. Zasada, J. Janas, W. Piskorz, M. Gorczynska, Z. Sojka, *ACS Catal.* 7 (2017)  
677 2853-2867. <https://doi.org/10.1021/acscatal.6b03139>.
- 678 [8] F. Zasada, W. Piskorz, J. Janas, J. Grybos, P. Indyka, Z. Sojka, *ACS Catal.* 5  
679 (2015) 6879-6892. <https://doi.org/10.1021/acscatal.5b01900>.
- 680 [9] L.F. Liotta, G. Di Carlo, G. Pantaleo, A.M. Venezia, G. Deganello, *Appl. Catal. B*  
681 *Environ.* 66 (2006) 217-227. <https://doi.org/10.1016/j.apcatb.2006.03.018>.
- 682 [10] Z. Pu, H. Zhou, Y. Zheng, W. Huang, X. Li, *Appl. Surf. Sci.* 410 (2017) 14-21.  
683 <https://doi.org/10.1016/j.apsusc.2017.02.186>.
- 684 [11] Z. Chen, S. Wang, W. Liu, X. Gao, D. Gao, M. Wang, S. Wang, *Appl. Catal. A*  
685 *Gen.* 525 (2016) 94-102. <https://doi.org/10.1016/j.apcata.2016.07.009>.
- 686 [12] Q. Wang, Y. Peng, J. Fu, G.Z. Kyzas, S.M.R. Billah, S. An, *Appl. Catal. B*  
687 *Environ.* 168-169 (2015) 42-50. <https://doi.org/10.1016/j.apcatb.2014.12.016>.
- 688 [13] G. Grzybek, K. Ciura, S. Wójcik, J. Gryboś, P. Indyka, M. Inger, K. Antoniak-  
689 Jurak, P. Kowalik, A. Kotarba, Z. Sojka, *Catal. Sci. Technol.* 7 (2017) 5723-5732.  
690 <https://doi.org/10.1039/C7CY01575E>.
- 691 [14] I. Zacharaki, C.G. Kontoyannis, S. Boghosian, A. Lycourghiotis, C. Kordulis,  
692 *Catal. Today* 143 (2009) 38-44. <https://doi.org/10.1016/j.cattod.2008.09.026>.

- 693 [15] B. Solsona, T.E. Davies, T. Garcia, I. Vázquez, A. Dejoz, S.H. Taylor, Appl.  
694 Catal. B Environ. 84 (2008) 176-184.  
695 <https://doi.org/10.1016/j.apcatb.2008.03.021>.
- 696 [16] L.F. Liotta, G. Pantaleo, A. Macaluso, G. Di Carlo, G. Deganello, Appl. Catal. A  
697 Gen. 245 (2003) 167-177. [https://doi.org/10.1016/S0926-860X\(02\)00652-X](https://doi.org/10.1016/S0926-860X(02)00652-X).
- 698 [17] J. Cheng, J. Yu, X. Wang, L. Li, J. Li, Z. Hao, Energ. Fuels 22 (2008) 2131-2137.  
699 <https://doi.org/10.1021/ef8000168>.
- 700 [18] S. Park, G. Kwak, Y. Lee, K. Jun, Y.T. Kim, Bull. Korean Chem. Soc. 39 (2018)  
701 540-547. <https://doi.org/10.1002/bkcs.11431>.
- 702 [19] J. Park, S. Yeo, T. Kang, I. Heo, K. Lee, T. Chang, Fuel 212 (2018) 77-87.  
703 <https://doi.org/10.1016/j.fuel.2017.09.090>.
- 704 [20] Y. Zhang, H. Xiong, K. Liew, J. Li, J. Mol. Catal. A Chem. 237 (2005) 172-181.  
705 <https://doi.org/10.1016/j.molcata.2005.04.057>.
- 706 [21] V. Garcilaso, J. Barrientos, L.F. Bobadilla, O.H. Laguna, M. Boutonnet, M.A.  
707 Centeno, J.A. Odriozola, Renew. Energ. 132 (2019) 1141-1150.  
708 <https://doi.org/10.1016/j.renene.2018.08.080>.
- 709 [22] M.A. Ulla, R. Spretz, E. Lombardo, W. Daniell, H. Knözinger, Appl. Catal. B  
710 Environ. 29 (2001) 217-229. [https://doi.org/10.1016/S0926-3373\(00\)00204-6](https://doi.org/10.1016/S0926-3373(00)00204-6).
- 711 [23] S. Ji, S. Ji, H. Wang, E. Flahaut, K.S. Coleman, M.L.H. Green, Catal. Lett. 75  
712 (2001) 65-71. <https://doi.org/10.1023/A:1016711207912>.
- 713 [24] A. Choya, B. de Rivas, J.R. González-Velasco, J.I. Gutiérrez-Ortiz, R. López-  
714 Fonseca, Appl. Catal. B Environ. 237 (2018) 844-854.  
715 <https://doi.org/10.1016/j.apcatb.2018.06.050>.
- 716 [25] A. Choya, B. de Rivas, J.I. Gutiérrez-Ortiz, R. López-Fonseca, Catalysts 8 (2018)  
717 427. <https://doi.org/10.3390/catal8100427>.
- 718 [26] K.M.S. Khalil, J. Colloid Interf. Sci. 307 (2007) 172-180.  
719 <https://doi.org/10.1016/j.jcis.2006.11.039>.
- 720 [27] Q. Yu, X. Wu, C. Tang, L. Qi, B. Liu, F. Gao, K. Sun, L. Dong, Y. Chen, J.  
721 Colloid Interf. Sci. 354 (2011) 341-352.  
722 <https://doi.org/10.1016/j.jcis.2010.10.043>.
- 723 [28] A. Martínez-Arias, M. Fernández-García, L.N. Salamanca, R.X. Valenzuela, J.C.  
724 Conesa, J. Soria, J. Phys. Chem. B 104 (2000) 4038-4046.  
725 <https://doi.org/10.1021/jp992796y>.
- 726 [29] B. de Rivas, C. Sampedro, E.V. Ramos-Fernández, R. López-Fonseca, J. Gascon,  
727 M. Makkee, J.I. Gutiérrez-Ortiz, Appl. Catal. A Gen. 456 (2013) 96-104.  
728 <https://doi.org/10.1016/j.apcata.2013.02.026>.

- 729 [30] M. Gil-Calvo, C. Jiménez-González, B. de Rivas, J.I. Gutiérrez-Ortiz, R. López-  
730 Fonseca, *Ind. Eng. Chem. Res.* 56 (2017) 6186-6197.  
731 <https://doi.org/10.1021/acs.iecr.7b00986>.
- 732 [31] Y. Ji, Z. Zhao, A. Duan, G. Jiang, J. Liu, *J. Phys. Chem. C* 113 (2009) 7186-7199.  
733 <https://doi.org/10.1021/jp8107057>.
- 734 [32] Q. Liu, L. Wang, M. Chen, Y. Cao, H. He, K. Fan, *J. Catal.* 263 (2009) 104-113.  
735 <https://doi.org/10.1016/j.jcat.2009.01.018>.
- 736 [33] D.K. Chlebda, R.J. Jędrzejczyk, P.J. Jodłowski, J. Łojewska, *J. Raman Spectrosc.*  
737 48 (2017) 1871-1880. <https://doi.org/10.1002/jrs.5261>.
- 738 [34] X. Jiang, Y. Ma, Y. Chen, Y. Li, Q. Ma, Z. Zhang, C. Wang, Y. Yang,  
739 *Spectrochim. Acta Part A Mol. Biomol. Spectrosc.* 190 (2018) 61-67.  
740 <https://doi.org/10.1016/j.saa.2017.08.076>.
- 741 [35] V. D'Ippolito, G.B. Andreozzi, D. Bersani, P.P. Lottici, *J. Raman Spectrosc.* 46  
742 (2015) 1255-1264. <https://doi.org/10.1002/jrs.4764>.
- 743 [36] Q. Zhang, S. Mo, B. Chen, W. Zhang, C. Huang, D. Ye, *Mol. Catal.* 454 (2018)  
744 12-20. <https://doi.org/10.1016/j.mcat.2018.05.006>.
- 745 [37] D. Li, L. Wang, M. Koike, Y. Nakagawa, K. Tomishige, *Appl. Catal. B Environ.*  
746 102 (2011) 528-538. <https://doi.org/10.1016/j.apcatb.2010.12.035>.
- 747 [38] G. Zou, Y. Xu, S. Wang, M. Chen, W. Shangguan, *Catal. Sci. Technol.* 5 (2015)  
748 1084-1092. <https://doi.org/10.1039/c4cy01141d>.
- 749 [39] R. Dziembaj, A. Chojnacka, Z. Piwowarska, M. Gajewska, M. Swietoslawski, S.  
750 Górecka, M. Molenda, *Catal. Today* 333 (2019) 196-207.  
751 <https://doi.org/10.1016/j.cattod.2018.03.042>.
- 752 [40] J. González-Prior, R. López-Fonseca, J.I. Gutiérrez-Ortiz, B. de Rivas, *Appl.*  
753 *Catal. B Environ.* 222 (2018) 9-17. <https://doi.org/10.1016/j.apcatb.2017.09.050>.
- 754 [41] M. Singh, N.K. Ralhan, S. Singh, *Bull. Mater. Sci.* 38 (2015) 297-301.  
755 <https://doi.org/10.1007/s12034-015-0872-5>.
- 756 [42] M.C. Biesinger, B.P. Payne, A.P. Grosvenor, L.W.M. Lau, A.R. Gerson, R.S.C.  
757 Smart, *Appl. Surf. Sci.* 257 (2011) 2717-2730.  
758 <https://doi.org/10.1016/j.apsusc.2010.10.051>.
- 759 [43] C. Tang, C. Wang, S. Chien, *Thermochim. Acta* 473 (2008) 68-73.  
760 <https://doi.org/10.1016/j.tca.2008.04.015>.
- 761 [44] Ming Meng, Y.Q. Zha, J.Y. Luo, T.D. Hu, Y.N. Xie, T. Liu, J. Zhang, *Appl.*  
762 *Catal. A Gen.* 301 (2006) 145-151. <https://doi.org/10.1016/j.apcata.2005.06.035>.

- 763 [45] H. Sohn, G. Celik, S. Gunduz, D. Dogu, S. Zhang, J. Shan, F. Feng Tao, U.S.  
764 Ozkan, *Catal. Lett.* 147 (2017) 2863-2876. <https://doi.org/10.1007/s10562-017->  
765 2176-4.
- 766 [46] L. Hu, Q. Peng, Y. Li, *J. Am. Chem. Soc.* 130 (2008) 16136-16137.  
767 <https://doi.org/10.1021/ja806400e>.
- 768 [47] A.W. Budiman, S. Song, T. Chang, C. Shin, M. Choi, *Catal. Surv. Asia* 16 (2012)  
769 183-197. <https://doi.org/10.1007/s10563-012-9143-2>.
- 770 [48] M. Gil-Calvo, C. Jiménez-González, B. De Rivas, J.I. Gutiérrez-Ortiz, R. López-  
771 Fonseca, *Chem. Eng. Trans.* 57 (2017) 901-906.  
772 <https://doi.org/10.3303/CET1757151>.
- 773 [49] N. Bahlawane, *Appl. Catal. B Environ.* 67 (2006) 168-176.  
774 <https://doi.org/10.1016/j.apcatb.2006.03.024>.
- 775 [50] P. Stefanov, S. Todorova, A. Naydenov, B. Tzaneva, H. Kolev, G. Atanasova, D.  
776 Stoyanova, Y. Karakirova, K. Aleksieva, *Chem. Eng. J.* 266 (2015) 329-338.  
777 <https://doi.org/10.1016/j.cej.2014.12.099>.
- 778 [51] A.K. Dalai, B.H. Davis, *Appl. Catal. A Gen.* 348 (2008) 1-15.  
779 <https://doi.org/10.1016/j.apcata.2008.06.021>.
- 780 [52] Ø Borg, Z. Yu, D. Chen, E.A. Blekkan, E. Rytter, A. Holmen, *Top. Catal.* 57  
781 (2014) 491-499. <https://doi.org/10.1007/s11244-013-0205-0>.
- 782  
783



784 **CAPTIONS FOR TABLES AND FIGURES**

- 785 Table 1. Physico-chemical properties of the xCe-Al supports.
- 786 Table 2. Physico-chemical properties of the Co/xCe-Al catalysts.
- 787 Table 3. Surface composition of the Co/xCe-Al catalysts as determined by XPS.
- 788 Table 4. Results from the H<sub>2</sub>-TPR and CH<sub>4</sub>-TPRe analysis of the Co/xCe-Al  
789 catalysts.
- 790
- 791 Figure 1. XRD profiles of the xCe-Al supports.
- 792 Figure 2. H<sub>2</sub>-TPR profiles of the xCe-Al supports.
- 793 Figure 3. XRD profiles of the Co/xCe-Al catalysts.
- 794 Figure 4. Raman spectra of the Co/xCe-Al catalysts.
- 795 Figure 5. HAADF-STEM images of the Co/xCe-Al catalysts coupled with EDX  
796 elemental distribution of Co (red), Ce (green) and Al (blue).
- 797 Figure 6. Evolution of the surface molar composition (XPS) and O<sub>2</sub> consumption  
798 (CH<sub>4</sub>-TPRe) with the Ce loading of the Co/xCe-Al.
- 799 Figure 7. H<sub>2</sub>-TPR profiles of the Co/xCe-Al catalysts.
- 800 Figure 8. CH<sub>4</sub>-TPRe profiles of the Co/xCe-Al catalysts (a). Close-up view of the  
801 300-550 °C temperature range (b).
- 802 Figure 9. Light-off curves of the Co/xCe-Al catalysts.
- 803 Figure 10. Specific reaction rate at 400 °C and O<sub>2</sub> consumption at low temperatures  
804 (CH<sub>4</sub>-TPRe) of the Co/xCe-Al catalysts.
- 805 Figure 11. Evolution of conversion with time on stream of the Co/20Ce-Al catalyst  
806 under dry conditions (450 °C/60 h and 525 °C/90 h) and cycling  
807 dry/humid conditions (525 °C/150 h).
- 808

| Sample                  | Ce,<br>% wt. | $S_{\text{BET}}$ ,<br>$\text{m}^2 \text{g}^{-1}$ | $V_{\text{pore}}$ ,<br>$\text{cm}^3 \text{g}^{-1}$ | Pore Size<br>Distribution maxima, Å | $D_{\text{CeO}_2}$ ,<br>nm | $\text{H}_2$ uptake,<br>$\text{mmol g}_{\text{Ce}}^{-1}$ |
|-------------------------|--------------|--|--|-------------------------------------|----------------------------|--|
| $\text{Al}_2\text{O}_3$ | -            | 139  | 0.56   | 110, 150                            | -                          | -  |
| 5Ce-Al                  | 5.2          | 128  | 0.51   | 110, 150                            | 10                         | 1.9  |
| 10Ce-Al                 | 9.8          | 126  | 0.51   | 110, 150                            | 9                          | 2.1  |
| 15Ce-Al                 | 15.3         | 122  | 0.49   | 110, 150                            | 10                         | 2.6  |
| 20Ce-Al                 | 20.6         | 117  | 0.42   | 110                                 | 12                         | 3.3  |
| 30Ce-Al                 | 30.3         | 105  | 0.32   | 35, 110                             | 12                         | 3.1  |
| $\text{CeO}_2$          | 81.4         | 8  | 0.03   | 230                                 | 32                         | 1.8  |

810

811

TABLE 1

812

| Sample                            | Ce,<br>% wt. | Co,<br>% wt. | $S_{\text{BET}}$ ,<br>$\text{m}^2 \text{g}^{-1}$ | $V_{\text{pore}}$ ,<br>$\text{cm}^3 \text{g}^{-1}$ | Pore Size<br>Distribution maxima, Å | $D_{\text{CeO}_2}$ ,<br>nm | $D_{\text{Co-spinel}}$ ,<br>nm |
|-----------------------------------|--------------|--------------|--|--|-------------------------------------|----------------------------|--------------------------------|
| Co/Al <sub>2</sub> O <sub>3</sub> | -            | 27.9         | 108  | 0.29   | 90                                  | -                          | 29                             |
| Co/5Ce-Al                         | 3.1          | 28.8         | 102  | 0.32   | 110                                 | 8                          | 24                             |
| Co/10Ce-Al                        | 5.9          | 28.9         | 96   | 0.30   | 110                                 | 9                          | 24                             |
| Co/15Ce-Al                        | 9.2          | 28.0         | 90   | 0.32   | 110                                 | 10                         | 23                             |
| Co/20Ce-Al                        | 12.4         | 29.5         | 93   | 0.30   | 90                                  | 11                         | 23                             |
| Co/30Ce-Al                        | 18.2         | 27.2         | 73   | 0.25   | 35, 110                             | 14                         | 31                             |
| Co/CeO <sub>2</sub>               | 48.8         | 28.9         | 18   | 0.07   | 225                                 | 33                         | 44                             |

813

814

TABLE 2

| Sample                            | Co,<br>% wt. | Ce,<br>% wt. | Al,<br>% wt. | Co/(Ce+Al)<br>molar ratio | Co <sup>3+</sup> /Co <sup>2+</sup><br>molar ratio | O <sub>ads</sub> /O <sub>latt</sub><br>molar ratio |
|-----------------------------------|--------------|--------------|--------------|---------------------------|---|--|
| Co/Al <sub>2</sub> O <sub>3</sub> | 22.6 (27.9)  | 0 (0)        | 32.1 (37.0)  | 0.32                      | 0.67  | 1.41   |
| Co/5Ce-Al                         | 26.7 (28.8)  | 1.3 (3.1)    | 23.6 (32.1)  | 0.51                      | 0.91  | 1.30   |
| Co/10Ce-Al                        | 30.4 (28.9)  | 2.4 (5.9)    | 20.1 (30.0)  | 0.68                      | 0.99  | 0.98   |
| Co/15Ce-Al                        | 30.1 (28.0)  | 3.0 (9.2)    | 19.4 (29.1)  | 0.69                      | 1.15  | 0.82   |
| Co/20Ce-Al                        | 32.9 (29.5)  | 3.8 (12.4)   | 17.2 (26.1)  | 0.84                      | 1.38  | 0.77   |
| Co/30Ce-Al                        | 29.7 (27.2)  | 5.3 (18.2)   | 18.4 (20.1)  | 0.70                      | 1.17  | 0.88   |
| Co/CeO <sub>2</sub>               | 35.6 (28.9)  | 26.8 (48.8)  | 0 (0)        | 3.26                      | 0.95  | 1.07   |

816 The values in brackets correspond to the bulk composition as determined by WDXRF.

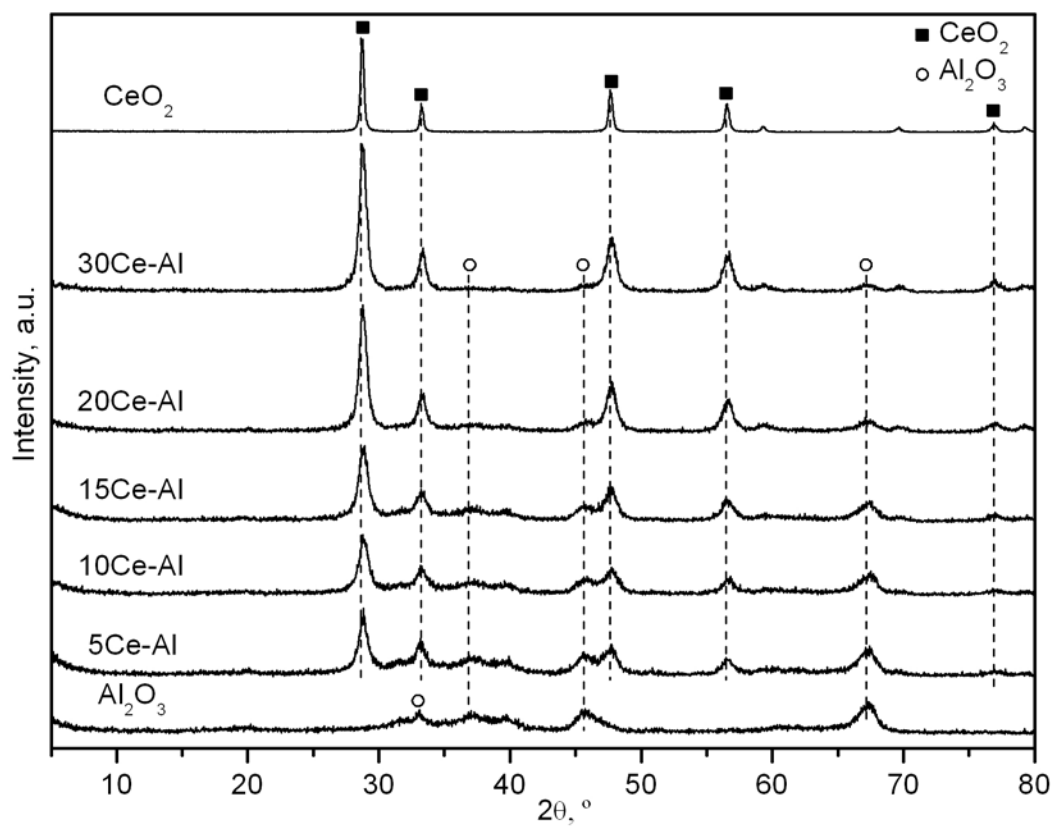
817

TABLE 3

818

| Sample                            | H <sub>2</sub> -TPR                   |                                       | CH <sub>4</sub> -TPRe                                   |
|-----------------------------------|---------------------------------------|---------------------------------------|---|
|                                   | H <sub>2</sub> uptake at low          | H <sub>2</sub> uptake at high         | O <sub>2</sub> consumption at                           |
|                                   | temperatures,<br>mmol g <sup>-1</sup> | temperatures,<br>mmol g <sup>-1</sup> | low temperatures,<br>mmol g <sub>Co</sub> <sup>-1</sup> |
| Co/Al <sub>2</sub> O <sub>3</sub> | 2.74                                  | 2.84                                  | 0.28  |
| Co/5Ce-Al                         | 2.01                                  | 3.86                                  | 0.45  |
| Co/10Ce-Al                        | 2.83                                  | 3.27                                  | 0.68  |
| Co/15Ce-Al                        | 3.02                                  | 3.22                                  | 0.72  |
| Co/20Ce-Al                        | 3.29                                  | 3.19                                  | 0.88  |
| Co/30Ce-Al                        | 3.68                                  | 2.61                                  | 0.77  |
| Co/CeO <sub>2</sub>               | 6.77                                  | 0.82                                  | 0.70  |

TABLE 4

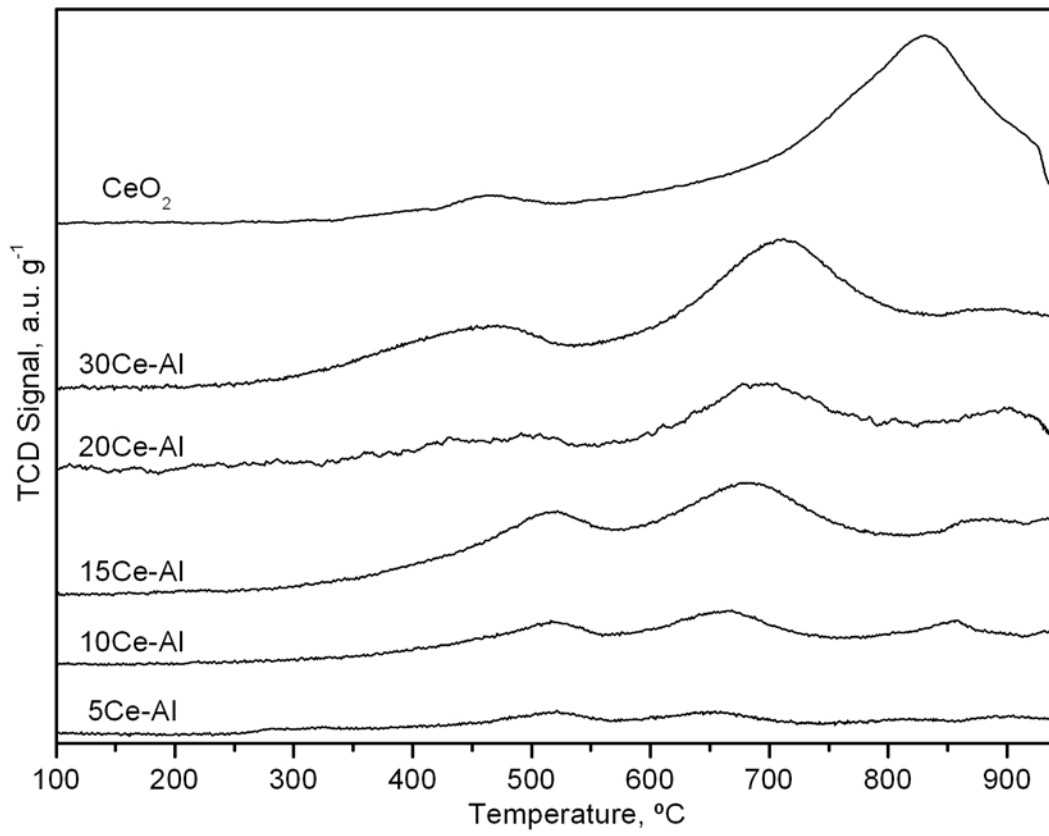


822

823

824

FIGURE 1

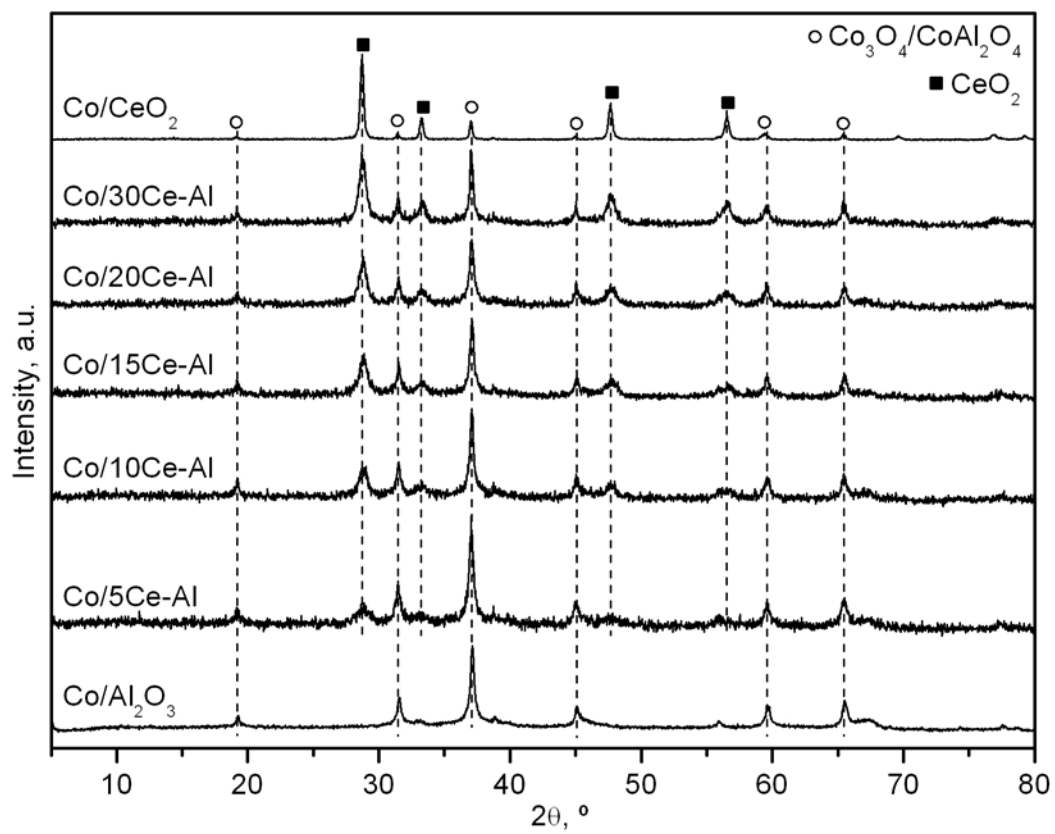


825

826

827

FIGURE 2



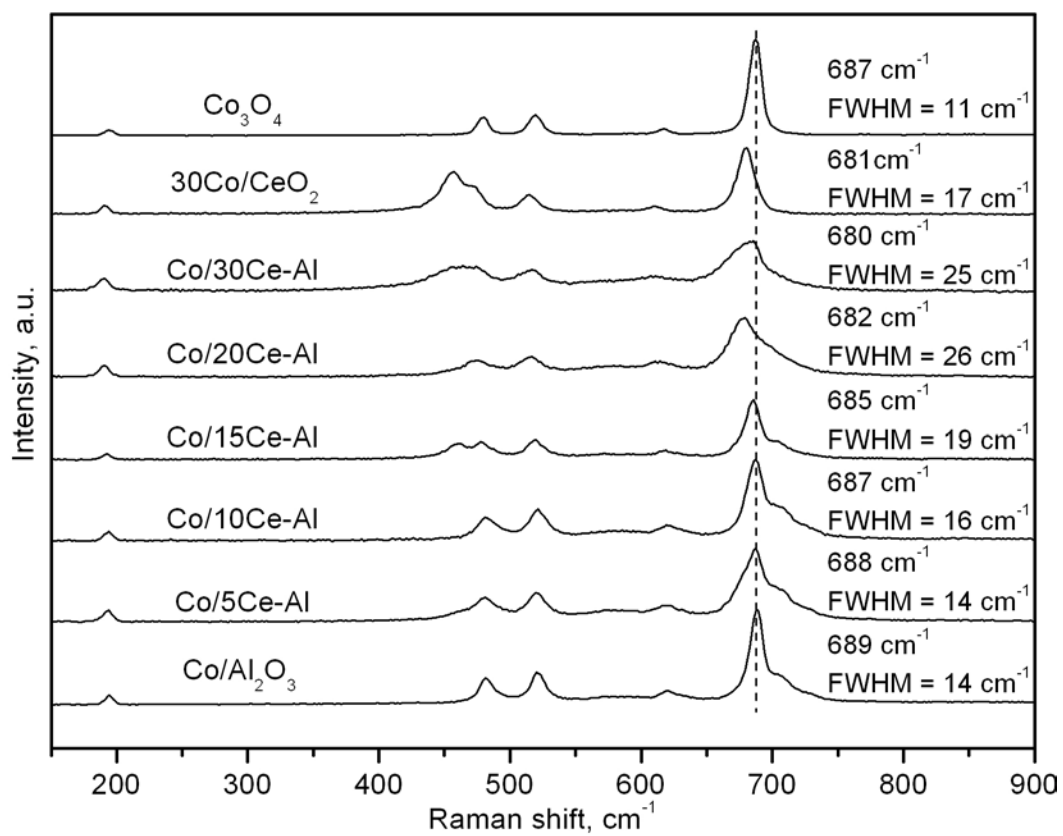
829

830

FIGURE 3

831



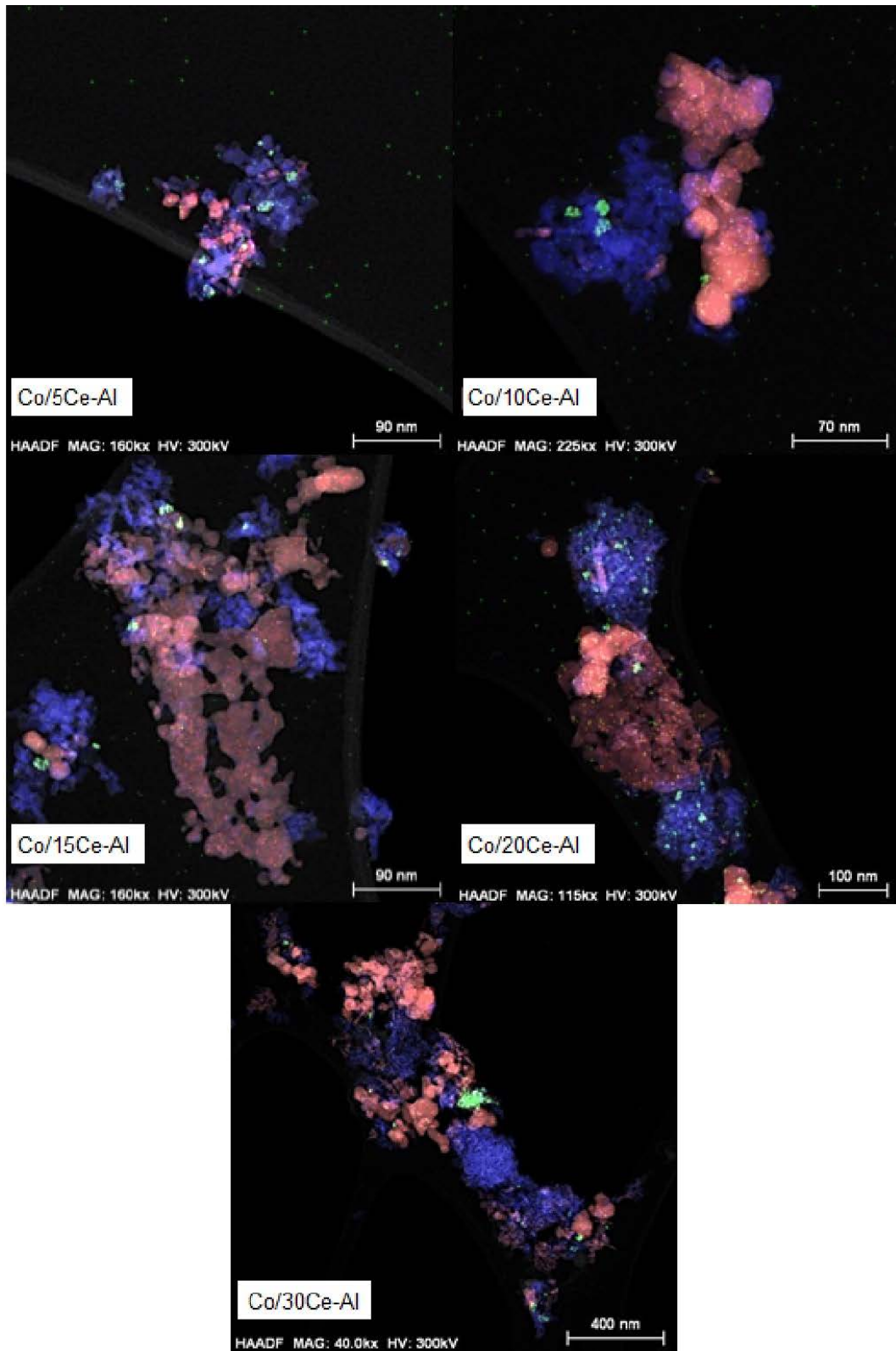


832

833

834

FIGURE 4

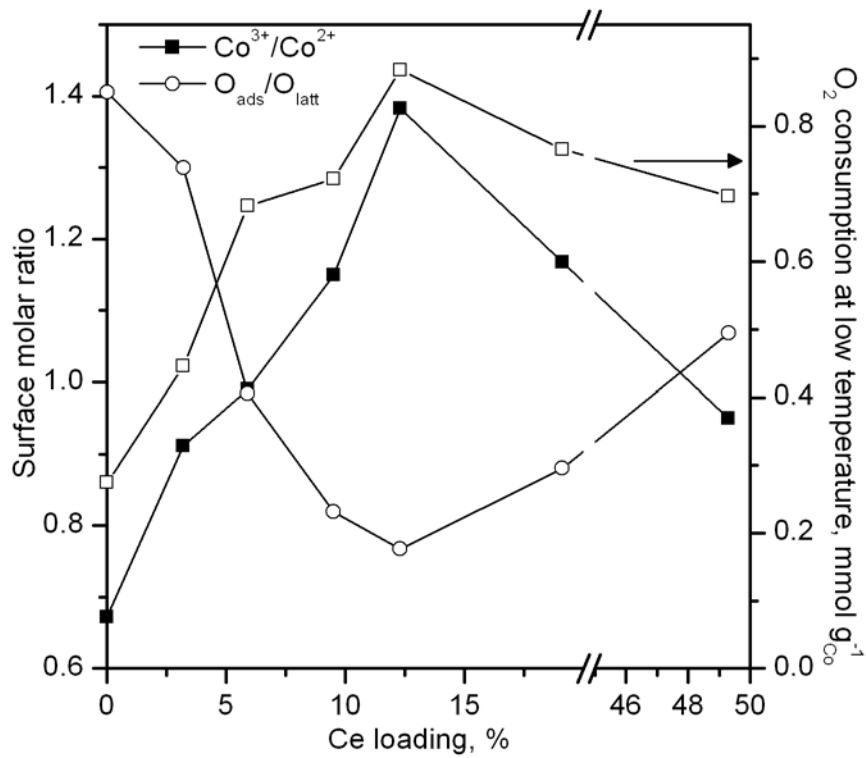


835

836

837

FIGURE 5

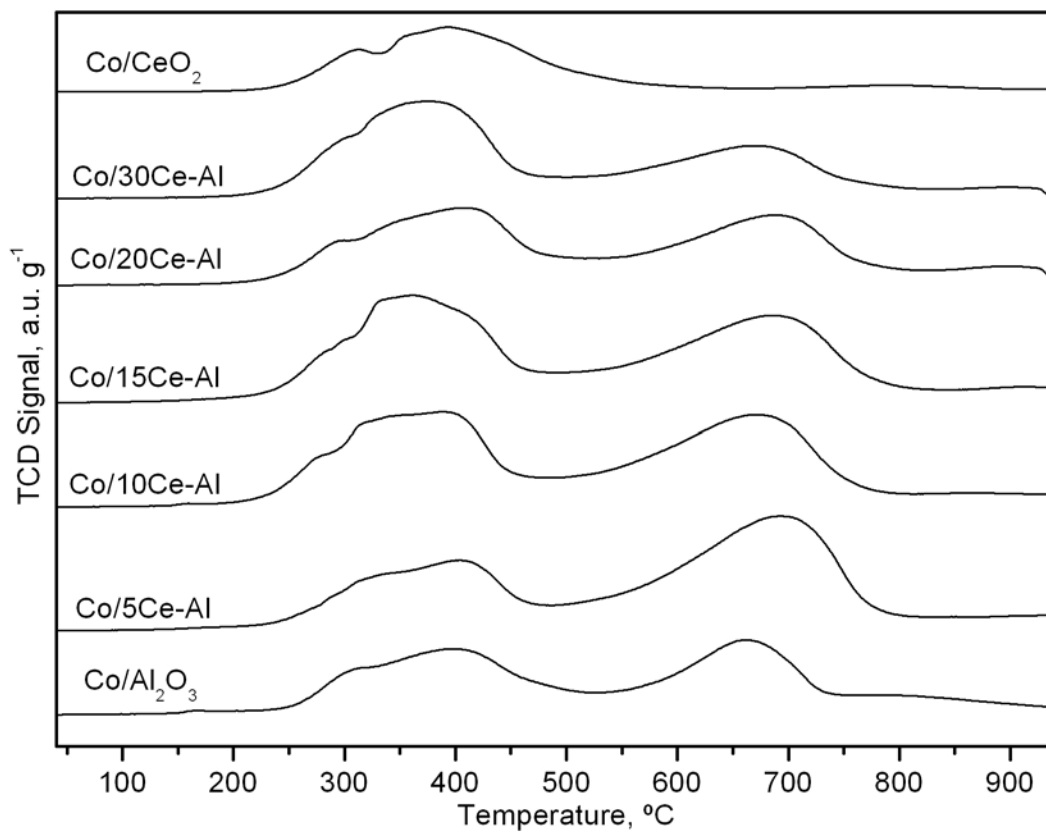


838

839

840

FIGURE 6

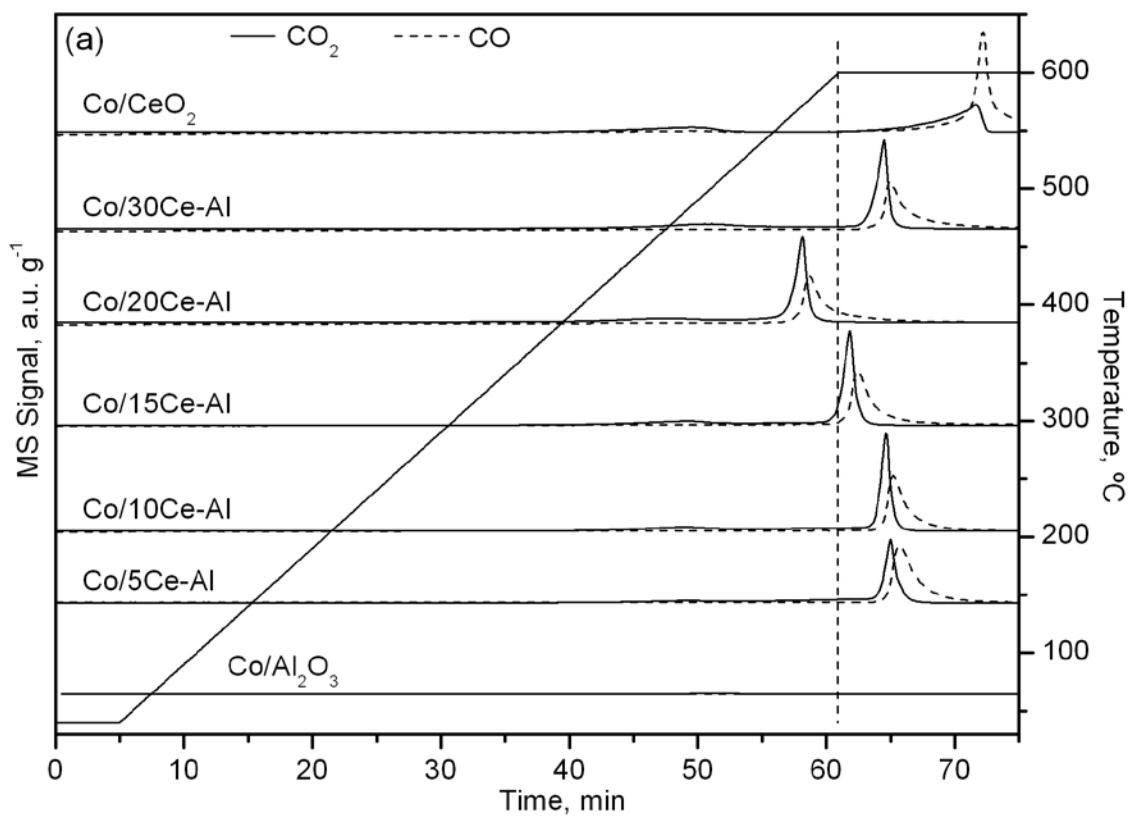


841

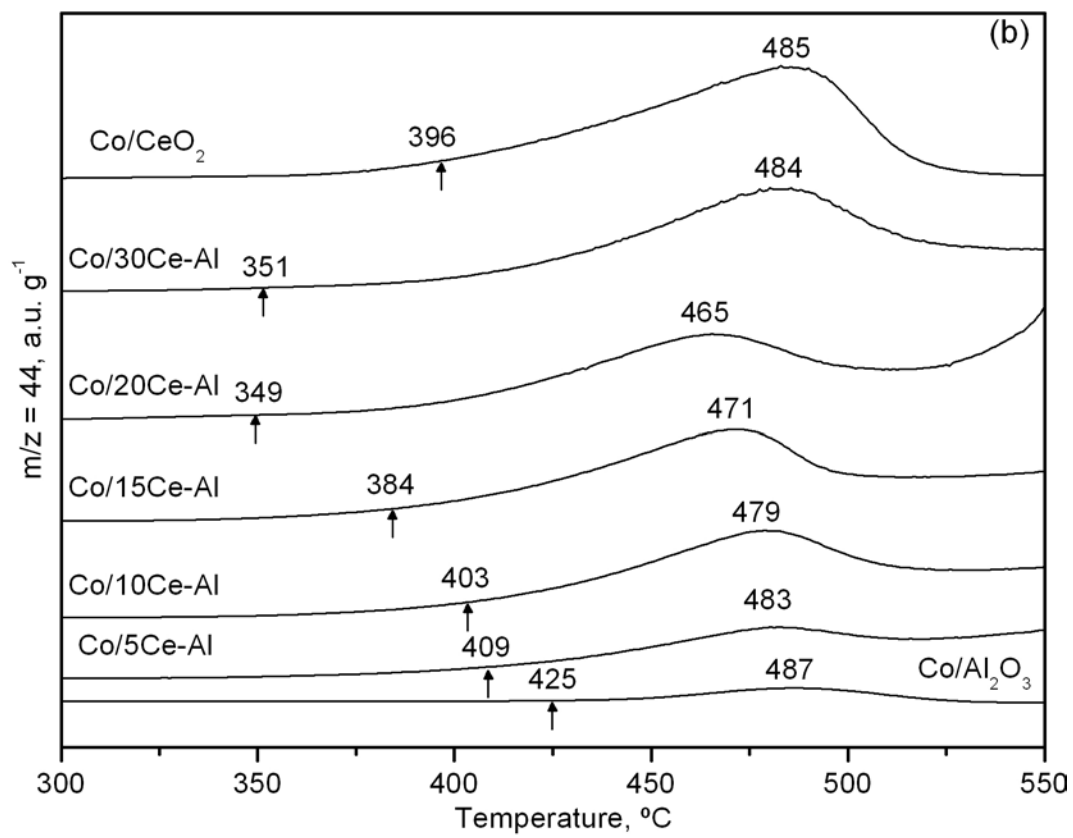
842

843

FIGURE 7



844

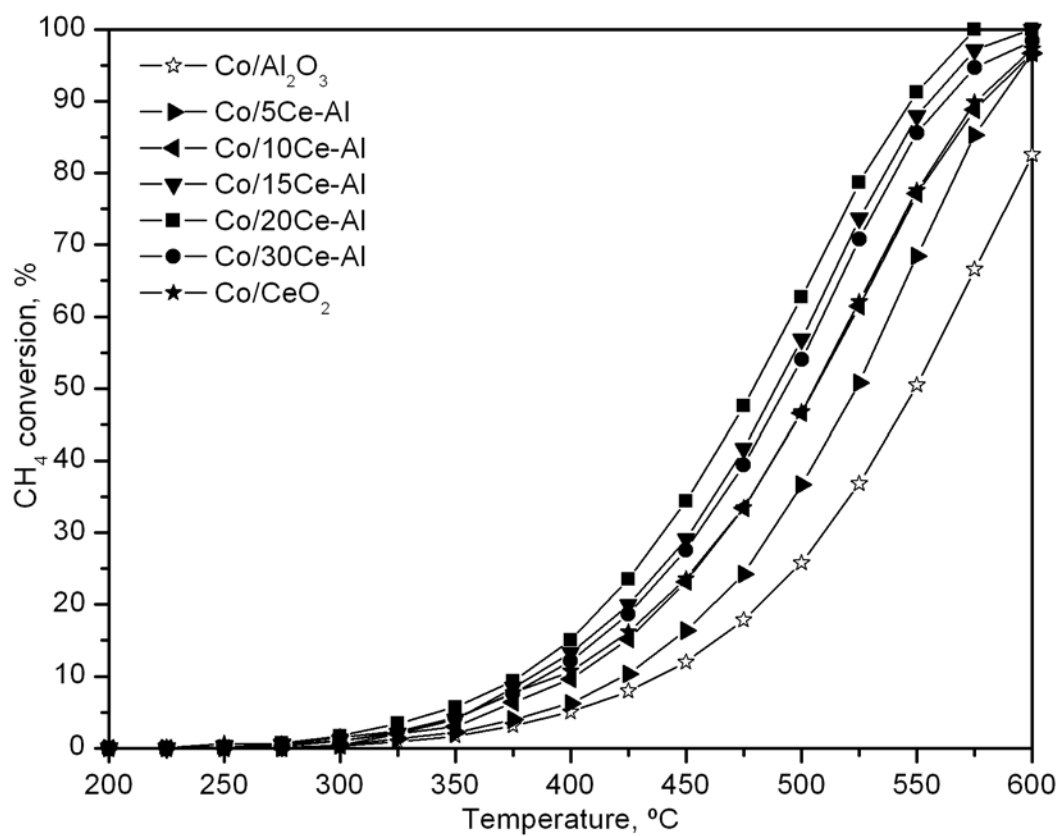


845

846

FIGURE 8

847



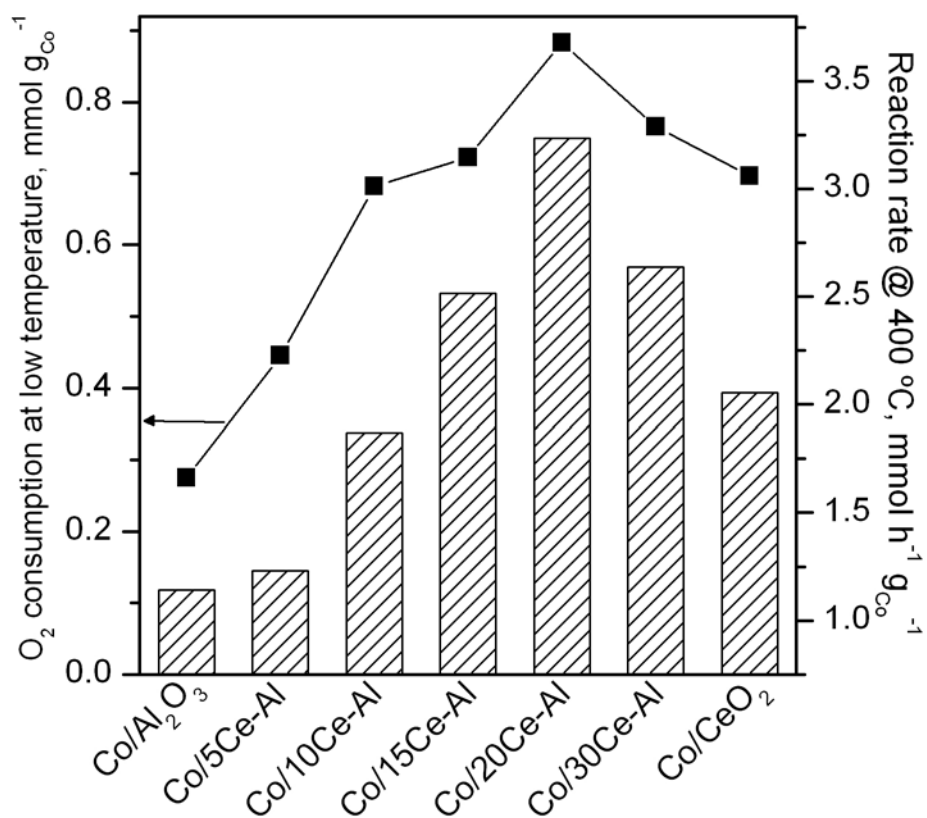
848

849

850

FIGURE 9

851

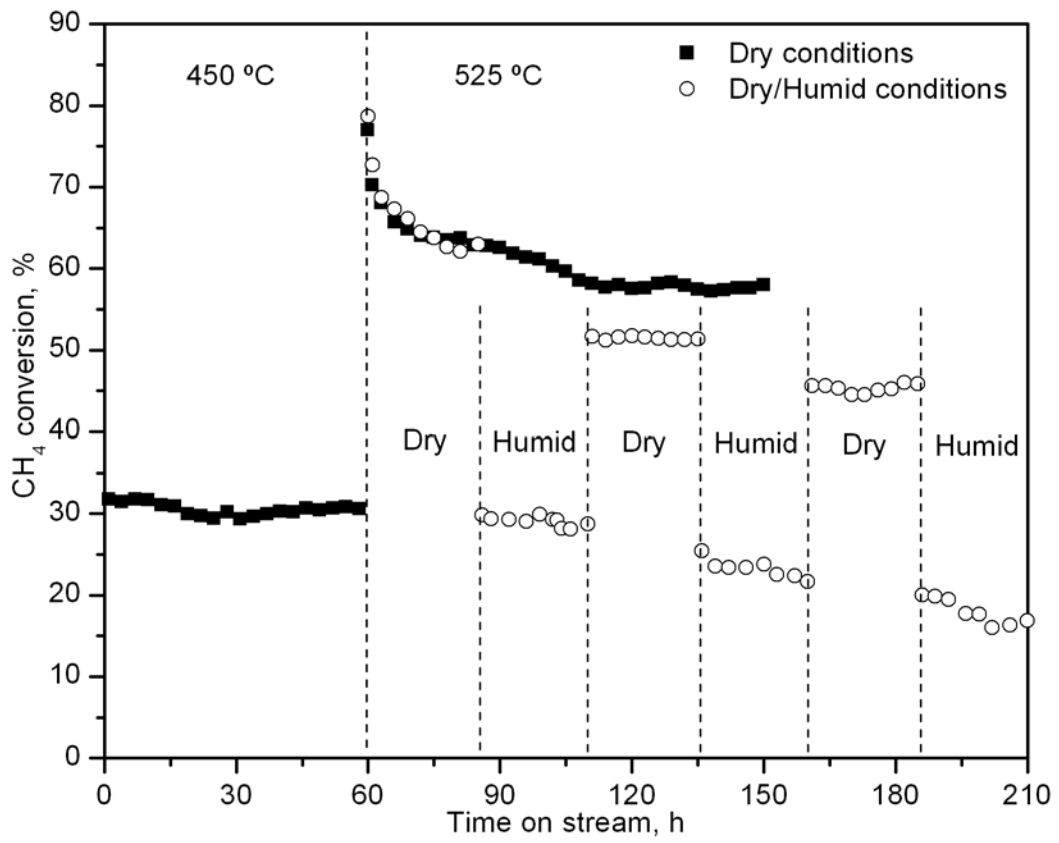


852

853

854

FIGURE 10



855

856

FIGURE 11